J. Fluid Mech. (1996), vol. 311, pp. 73–118

The evolution of a jet with vortex-generating tabs: real-time visualization and quantitative measurements

By M. F. REEDER AND M. SAMIMY

The Ohio State University, Department of Mechanical Engineering, Columbus,
OH 43210-1107, USA

(Received 4 March 1995 and in revised form 6 October 1995)

An experimental study involving flow visualization and two-component LDV measurements has been undertaken to elucidate the deformation of an axisymmetric jet ($Re_D \approx 1950$ and 4160) caused by tabs placed at the nozzle exit. Previous studies have shown the profound distortion of high-speed jets with tabs and have demonstrated that a pair of counter-rotating streamwise vortices generated by each tab are responsible for the deformation of the jet core. This work illustrates the distortion as well as some of the more subtle features of the tab effect. Extensive visualizations taken simultaneously from two perspectives reveal the real-time evolution of complex three-dimensional flow structures. Velocity data show the expected overall distortion, and the existence and strength of the streamwise vortices responsible for this deformation. Furthermore, a second set of weaker streamwise vortices was detected near each tab, the size and location of which was consistent with a horseshoe vortex system. The data showed a widespread increase in both Reynolds normal and shear stresses and generally indicated the accelerated development of the mixing layer when tabs were inserted. A brief analysis employing vortex dynamics – an alternative to previous work which utilized pressure gradient arguments – is used to explain the tab effect, resulting in similar conclusions.

1. Introduction

For applications ranging from military aircraft performance to environmental concerns, increased mixing of jet flows is of paramount interest. One of the more commonly used methods of attaining better mixing is to generate streamwise vortices which work to entrain ambient fluid into the jet. The presence and nature of streamwise vortices in axisymmetric jets, planar mixing layers, and boundary layers have been the focus of much experimental and analytical research. Understanding the mechanisms of formation, evolution, and interaction with Kelvin–Helmholtz-type vortices is also of great importance for such applications as well as from the viewpoint of fundamental fluid physics.

The focus of this work is the effect of tabs, which are simple protrusions into the flow located at the exit of a nozzle, on the evolution of a jet. Previous work (Bradbury & Khadem 1975; Ahuja & Brown 1989) has established that even relatively small tabs cause dramatic distortion of a jet. In a series of experiments, Samimy, Zaman & Reeder (1993) and Zaman, Reeder & Samimy (1994) confirmed the overall tab effect and showed that a pair of counter-rotating streamwise vortices generated by each tab were responsible for the witnessed distortion. In contrast to this earlier work, the present study was conducted for relatively low-speed jets ($U_j = 0.16$ m s^{-1}) in order to observe in close detail the combined effects of streamwise vortices and jet instabilities on the mixing.

1.1. *General mixing layer observations*

Spanwise coherent vortical structures resulting from the Kelvin–Helmholtz instability are known to exist for both relatively low (e.g. Winant & Browand 1974) and high Reynolds number (e.g. Brown & Roshko 1974) planar mixing layers. In the axisymmetric case, these structures take the form of fairly well-defined rings for relatively low Reynolds number jets (e.g. Yule 1978) and large-scale axisymmetric and helical structures for highly turbulent jets (e.g. Crow & Champagne 1971; Dimotakis, Miake-Lye & Papantoniou 1983; Yoda, Hesselink & Mungal 1992). The existence of a highly two-dimensional structure in a turbulent mixing layer is striking. As Cantwell's (1981) review article points out, the breakdown of a flow into turbulence had traditionally been argued based on vortex stretching. If that were the sole mechanism responsible, one might expect that any structures of spanwise vorticity would quickly be dominated by streamwise vorticity in a free shear layer. Evidence of the persistence of these spanwise structures and the potential use of large-scale structure growth to enhance mixing and entrainment sparked renewed interest in the study of turbulent mixing.

While the coherent structures in planar mixing layers are often referred to as two-dimensional, there exist spanwise non-uniformities which add complexity to the nature of evolving free shear layers. Konrad (1976) and Breidenthal (1981) observed streamwise streaks in flow visualizations, and Browand & Troutt (1980) noted spanwise irregularities in a plane mixing layer which they attributed to the pairing interaction of adjacent vortices. Jimenez (1983) also observed deformations and suggested that a secondary instability was responsible for the generation of streamwise vortical structures in the layer. Bernal & Roshko (1986) used flow visualizations to construct a topology of streamwise vortex lines.

Theoretical analyses and numerical simulations similarly indicate a proclivity for streamwise structure formation. Pierrehumbert & Widnall (1982) analysed a periodic row of Stuart vortices and showed that a mode of instability allows growth of these vortices along the spanwise vortex cores. Corcos & Lin (1984) showed that even without the periodic pattern employed by Pierrehumbert & Widnall, sheets of streamwise vorticity will collapse into concentrated round vortex filaments as long as the initial spanwise vorticity is deformed. Ashurst & Meiburg (1988) partially accounted for the incoming boundary layers by adding the complication of initial spanwise vorticity of opposite signs emanating from the splitter plate. They also found that many aspects of the initial stages of mixing layer development can be understood using inviscid vortex dynamics. Martin & Meiburg (1991) extended these planar analyses to the case of an axisymmetric evolving jet using vortex dynamics. It should be remarked that each of these analyses are for temporally evolving cases and may not capture some nuances of a spatially evolving layer.

The original source of the streamwise vorticity and where it is amplified and becomes an integral part of the mixing process are of considerable interest in the present inquiry. Jimenez (1983) recognized that while the streamwise vorticity was spatially stationary for a particular case, the sites of streamwise vorticity generation were greatly influenced by upstream disturbances. Specifically, small bumps at the splitter plate edge corresponded spatially with spanwise non-uniformities, and it was inferred that these small bumps were associated with streamwise vortices which formed downstream. Lasheras, Cho & Maxworthy (1986) used flow visualizations to further illustrate the importance of upstream disturbances, and also found that the location where the streamwise vortices formed varied from just before the first spanwise roll-up to as late as the second or third spanwise roll-up. Bell & Mehta (1992) quantitatively showed that the streamwise vorticity in their two-dimensional mixing layer was amplified just after the first spanwise roll-up. In both of these cases and that of Bernal & Roshko (1986), the researchers found that the disturbances were first noticeable in the braid region although some numerical work has suggested the possibility of streamwise vorticity production in spanwise roller cores as well. In circular jets similar observations have been made in both experimental (Liepmann & Gharib 1992) and numerical work (e.g. Martin & Meiburg 1991).

Highly three-dimensional perturbations of mixing layers have been shown to generate strong streamwise vortices. Lasheras & Choi (1988) experimented with a sinusoidal corrugated splitter plate and found that both streamwise vortex tubes and spanwise roll-up occurred, suggesting an uncoupled development of both at locations near the splitter plate. Further downstream, they showed that coupling of streamwise and spanwise vorticity does take place. Lasheras *et al.* (1986) also collected images displaying the effects of projecting a cylinder into the high-speed stream at the spanwise centre of the splitter plate just upstream of the trailing edge. Bell & Mehta (1993) have explored the evolution of streamwise vortices caused by similar disturbances located upstream of the trailing edge of a splitter plate.

While free jets are similar in many ways to planar mixing layers, there are fundamental differences which arise from the decay of the jet core. This is primarily manifested in a column (or preferred) mode of instability existing alongside the Kelvin–Helmholtz roll-up. The length scale associated with the column mode is the jet diameter while that of the initial Kelvin–Helmholtz roll-up is the exit boundary layer momentum thickness. The overall effects of perturbations designed to generate streamwise vorticity have been explored for axisymmetric jets in a number of previous works. Axisymmetric nozzles with indeterminate origin have been scrutinized for subsonic jets (Longmire, Eaton & Elkins 1992). Supersonic jets with lobed nozzles (Tillman, Paterson & Presz 1992) as well as shock-generated disturbances (Wishart, Krothapalli & Mungal 1993) have been shown to produce strong effects. Reeder & Zaman (1994) have shown that the streamwise location of a cylindrical protrusion is crucial to the ultimate distortion of axisymmetric jets, particularly in underexpanded (supersonic) cases.

1.2. *Observed effects of tabs in jets*

According to the lore of the engineering and scientific community, the original concept of tabs was brought about serendipitously. Apparently, a technician observing the schlieren image of a supersonic jet pointed to a feature at the jet exit with a screwdriver. To the surprise of the researchers, the screech tone generated by the supersonic jet suddenly disappeared and the schlieren image changed dramatically when the screwdriver projected slightly into the flow.

As one might expect, this simple technique of eliminating screech has been known about and implemented for many years (Tanna 1977), yet thorough scientific analysis of the 'tab effect' has been somewhat scant. The first such investigation of which the authors are aware was performed by Bradbury & Khadem (1975), who examined the effect of two rectangular tabs located 180° apart which projected normally into a subsonic jet at the exit plane of the nozzle. While the tabs extended only 0.05 diameters into the flow, the resulting deformation of the flow pattern was dramatic. The streamwise velocity distribution indicated two peak regions on either side of the tabs with a trough at the centre of the jet. Bradbury & Khadem also probed the effect of

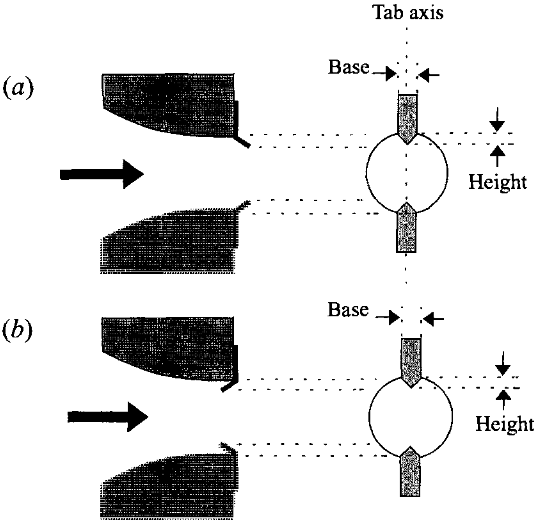

FIGURE 1. Sketch of the tabs used throughout the experiments. (*a*) Delta tabs, the base width is $0.28D$, and the height (as shown) is $0.10D$, angle = 135°. (*b*) Inverted delta tabs, base width = $0.28D$, height = $0.10D$, angle = 45°. The tab axis is indicated in (*a*).

replacing the tabs with ramps and found that tabs were far superior in distorting the jet. They argue that variations in flow angle at the exit are the primary reason why tabs are more effective than ramps. This is essentially correct, but additional reasoning employing vortex dynamics is presented in this text which should enhance understanding. In more recent work, Ahuja & Brown (1989) showed that the splitting of the jet into two high-velocity cores by the tabs also occurs in underexpanded axisymmetric jet cases for both cold and heated flows.

A wealth of information for various tab configurations and flow conditions has been obtained by Samimy *et al.* (1993), Zaman *et al.* (1994), Zaman (1993), and Reeder & Zaman (1994). Figure 1 shows general sketches of two tab configurations studied in detail in these references and also employed in the present work: 'delta' tabs, and 'inverted delta' tabs. Delta tabs, which are triangular with a wide base and angled downstream, were shown during the course of this series of experiments to produce a greater effect per unit blockage area when compared to simple rectangular tabs. The blockage area per tab was 1.4% of the total nozzle exit area. Inverted delta tabs have exactly the same shape and dimensions as delta tabs but the orientation of the tab tip is upstream. Details of the dimensions are given in the captions, and characteristics of the setup are noted in §2. Flow visualizations (Zaman *et al.* 1994) indicated that inverted delta tabs generate a second pair of streamwise vortices with a sense of rotation opposite that of the delta tabs. These vortices, located near the tab tip, tend to eject fluid outward from the jet core. One of the more interesting findings of earlier work was that a gap equal to the width of the tab drastically diminishes the effect. It was also observed that the effect of tabs was similar for subsonic and supersonic jets. This was a motivating factor in performing the water tunnel experiments of the present work since both experimentation and the equations governing the flow are much simpler.

In Zaman *et al.* (1994) the authors offer an explanation of the tab effect using pressure gradient arguments. In this text, an alternative explanation for incompressible cases utilizing vortex dynamics is put forth. This complements the previous work, and

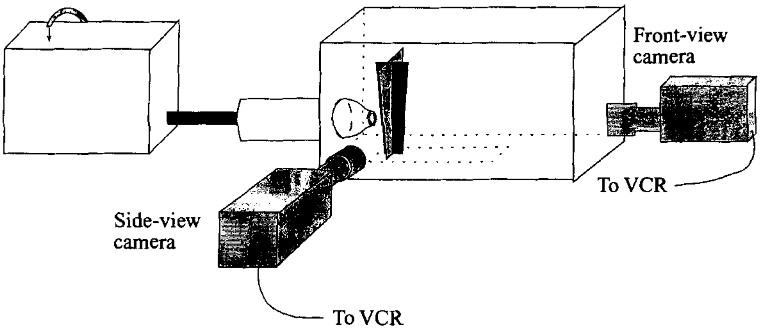

FIGURE 2. Sketch of the water tunnel and the set-up for the dual-view real-time flow visualizations.

it should be stressed that the two descriptions may generally be considered concurrently as explained in §4.

2. Experimental facility

The experimental facility is a water tunnel which was designed and constructed at the Aeronautical and Astronautical Research Laboratory (AARL) at the Ohio State University. The set-up, along with the arrangement for the flow visualizations, is shown in figure 2. A steady stream of water, monitored using a volumetric flowmeter, issues into the source tank. Gravity drives water from the source tank to a small settling chamber, and it eventually passes through a smooth nozzle into a clear ambient tank. The ambient tank itself was purchased off the shelf as a Plexiglas fishtank, and various modifications were since made. The contoured nozzle used throughout the experiments had a contraction ratio of 3:1 and became straight near the exit, which had a diameter D of 1.5 cm. The flow exited the nozzle parallel to the sidewalls of the ambient tank. The ambient tank is 91 cm long, 37 cm wide, and 38 cm high. The centre of the jet was 8.5 diameters above the bottom surface and roughly 12 diameters from each side. During the experiment the surface level varied but was maintained at least 6 diameters above the jet centreline. Since the area ratio of the source tank to the ambient tank did not vary appreciably with the water level, a steady flow could be maintained. The flow rate into the source tank was kept at 0.58 ± 0.01 gallons per minute, as monitored by the volumetric flowmeter, throughout all of the experiments. The tabs were pressed tightly against the nozzle face using a retainer ring.

The temperature of the water was maintained at 53 °F $\pm$ 2 °F for most of the cases. However, some measurements with an elevated water temperature ($T = 117$ °F) were also recorded to assess the flow at a higher Reynolds number while maintaining the same jet core velocity.

Flow visualization was performed on the jet using laser-induced fluorescence of fluorescein dye. The dichlorofluorescein indicator prepared in a solution of 70% ethanol has the property of fluorescing green when illuminated by blue (488 nm) light. Only a small amount of the dye mixed into the source tank was needed to mark the jet.

The source tank was seeded with dichlorofluorescein of variable concentrations such that the jet core was bright when illuminated by a sheet of light optically spread from the laser. The beam of wavelength 488 nm from the laser causes the fluorescein to fluoresce at roughly 500–600 nm. The fluorescing image was captured by VHS video cameras with 514.5 nm cut-off filters placed over the lens. The filters serve to block out the background light but allow most of the desired image to pass through. This filter permitted visualizations without having to separate the 514.5 nm and 488 nm wavelength beams of the argon laser. The shutter speed of the cameras was set at 1/4000 s, and the framing rate is a constant 30 frames per s. Each frame consists of two image fields which resulted in 60 recorded images per second. The low speed of the jet allowed the instantaneous features of the jet to be illuminated as they evolved in time. Time-averaged pictures were obtained using a 35 mm camera with a 1 s exposure.

To better capture the highly three-dimensional flow pattern induced by the tabs, a novel twist to the traditional planar laser-induced fluorescence (PLIF) flow visualization technique was employed. Instead of using one camera to record either streamwise or cross-sectional planar images, two ordinary video cameras were used simultaneously to record streamwise and spanwise views. These images were secured by splitting the beam and passing the two perpendicular sheets through the jet from the bottom of the ambient tank as shown in figure 2. The two cameras were synchronized to within 1/120 s by quickly blocking and unblocking the original laser beam while recording and adjusting the videotapes accordingly during review. The resulting real-time 'dual view' of the instantaneous features of the flow as the jet evolved quite effectively displays the structural dynamics of the mixing.

Two-component velocity measurements using laser Doppler velocimetry (LDV) were obtained in the water tunnel. The Spectra Physics model 20-5 5 W argon–ion laser was used to provide a coherent light source for the LDV system. The green (514.5 nm) and blue (488 nm) beams were separated, split, and then launched through 10 m fibreoptic cables to a TSI model 9275-1 probe. A TSI model 9167 250 mm lens with a 5.52° half-angle was placed on the probe to focus the four parallel beams to a point which formed the measurement volume. The four beams were projected through a glass sidewall of the ambient tank into the water, and backscattered light was collected by a receiving optic fibre within the probe. The length and breadth of the probe volume may be calculated using empirical relationships provided by TSI and are approximately 300 μm and 100 μm, respectively.

It was necessary to shift the frequency of both a blue beam and a green beam before launching them into the fibreoptic system in order to differentiate flow direction and reduce fringe bias. Two TSI model 9182-3A acousto-optic Bragg cell frequency shifters were used for this purpose. In essence, the shifted frequency results in an apparent motion of the fringes relative to the particles in the flow. For these experiments the frequency was shifted 50 kHz for both beams. The backscattered light was transmitted through the receiving cable, and then the colours were separated and passed into two TSI 9162 photomultiplier tubes. These tubes amplified the scattered light and converted it to an electronic signal. The signal was transmitted to a TSI IFA 750 digital burst correlator which converted the frequency of the intensity fluctuations to velocities. Two thousand data points were recorded for the average velocity and Reynolds stress measurements at each location at a data rate which varied from approximately 100 to 800 measurements per second. While some signal was present due to particles present in tap water, the data rate was increased by adding particles to both the source and ambient tanks. Both tanks were seeded in order to maintain spatial uniformity of the particles as much as possible. The supplementary particles used were Potters Industries Incorporated Sphericel™ hollow glass spheres of 8 μm diameter having a specific gravity of 1.1. The data rate, which was at least an order of magnitude higher than the time scales of the flow, permitted additional LDV measurements which were obtained in real time for spectral data using LDV. For these measurements, which are discussed in §3.5.2, the data rate was increased to at least 300 Hz, and between 6000 and 10000 data points were recorded.

An API 315X indexer was used in conjunction with a motor and a linear encoder to automatically move the fibreoptic probe across the jet test section. The motor was accessed through a serial port of a 486 50 MHz computer, which was also used to store velocity data. The encoder ensured the vertical location of the probe volume to within ±0.0002 in. ($0.0004D$). The second axis was manipulated by hand with an accuracy of ±0.002 in. ($0.004D$). The computer was connected to the burst correlator, and the sequence of taking data and subsequently moving the probe was generally managed from within a software package (FIND) provided by TSI. Additional details about the measurements taken with LDV are described in later sections as needed.

The tabs used in these experiments were of the same size and shape as those of previous work and are sketched in figure 1. Throughout this text, when two tabs are used, an imaginary line connecting each tab base is denoted the 'tab axis'. This is shown with an arrow in figure 1(*a*). The notation used for the secondary axes is arbitrary to some extent. Although the axisymmetric nature of the nozzle implies axisymmetric coordinates, Cartesian coordinates are generally used throughout the text for two reasons: the tabs disrupt the jet to the extent that Cartesian coordinates more readily apply; and Cartesian units are simpler. In this text, where tab cases are discussed, the tab axis is denoted y. The z-axis direction follows (with the x-direction, of course, showing the flow direction of the jet) using the right-hand rule. This is consistent with notation of earlier work.

3. Experimental results

3.1. *Time-averaged laser sheet flow visualizations*

The overall effect of tabs on the flow emanating from an axisymmetric nozzle may be considered using flow visualizations of the jet cross-sections. A comparison of various tab cases in the water tunnel, where the jet core is seeded with fluorescein and appears bright, is shown in figure 3. These time-averaged images, taken at $x/D = 2$ with a 35 mm camera with a 1 s exposure, clearly show the distortion of a jet with tabs. The tabs project into the flow from the top and bottom of the nozzle, as viewed in these images. The unperturbed jet, with $Re_D = 1950$, is shown in (*a*), the delta tab case in (*b*), and the inverted delta tab case in (*c*). The Reynolds number was calculated using the nozzle diameter, the dynamic viscosity of water at 53 °F, and the reference velocity $0.16\ \mathrm{m\ s^{-1}}$, which was the value of the velocity within the jet core. Given slight uncertainties in the temperature and velocity, this value for Re should be taken ±50. The jet without tabs exhibits an essentially circular cross-section, corresponding to the nozzle exit. Each of the tab cases, in which the two tabs were inserted from either side as sketched and pressed tightly against the nozzle face, shows a profound distortion of the jet. Along the tab axis there is a clear indentation into the exiting flow for each case. The inverted delta tab case exhibits many of the same features that the delta tab case does, except that there is a slight ejection of core fluid within the indentation. This small but important feature is pointed out in (*c*) with a white arrow. These average images are consistent with earlier work in high-speed jets.

3.2. *Mean streamwise velocity results*

Profiles of U, based on an average of 2000 points, at various streamwise locations for the low temperature no-tab case are given in figure 4(*a*). It can be seen that the initial velocity profile resembles a top hat, but as the jet evolves downstream additional fluid

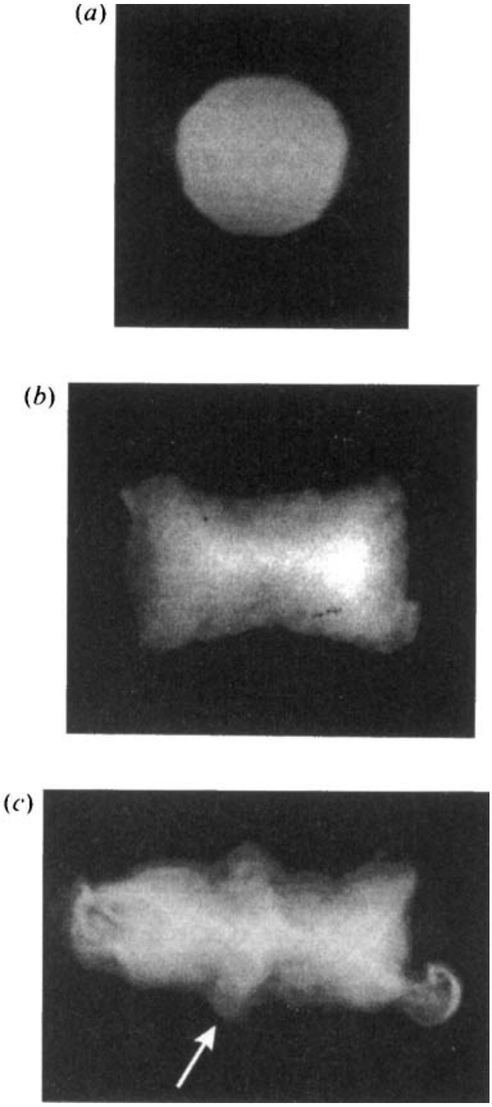

FIGURE 3. Time-averaged visualizations of an incompressible (Re = 1950) jet: (*a*) without tabs, with (*b*) with two delta tabs, and (*c*) with two inverted delta tabs. The tab axis, for each of these images, is vertical. The arrow in (*c*) marks the ejection of fluid near the tip of one of the inverted delta tabs.

is entrained and the mixing layer grows, as expected. Histograms taken across the jet showed well-behaved Gaussian distributions of the velocity for each radial position. The exit boundary layer properties were estimated from the measurements closest to the nozzle ($x/D = 0.15$). These data, along with the mixing layer thickness (estimated by averaging the thickness of the layers on either side of the jet) for each location, are given in table 1. Here, the centreline reference velocity is 0.16 m s^{-1}. The shape factor (H) of 2.83 indicates that the exit boundary layer is laminar.

A lateral traverse near the nozzle exit for the high-temperature case is compared to the lower temperature case in figure 4(*b*). Raising the temperature lowers the viscosity of water, thereby raising Re from 1950 to 4160 for a jet with the same flow rate.

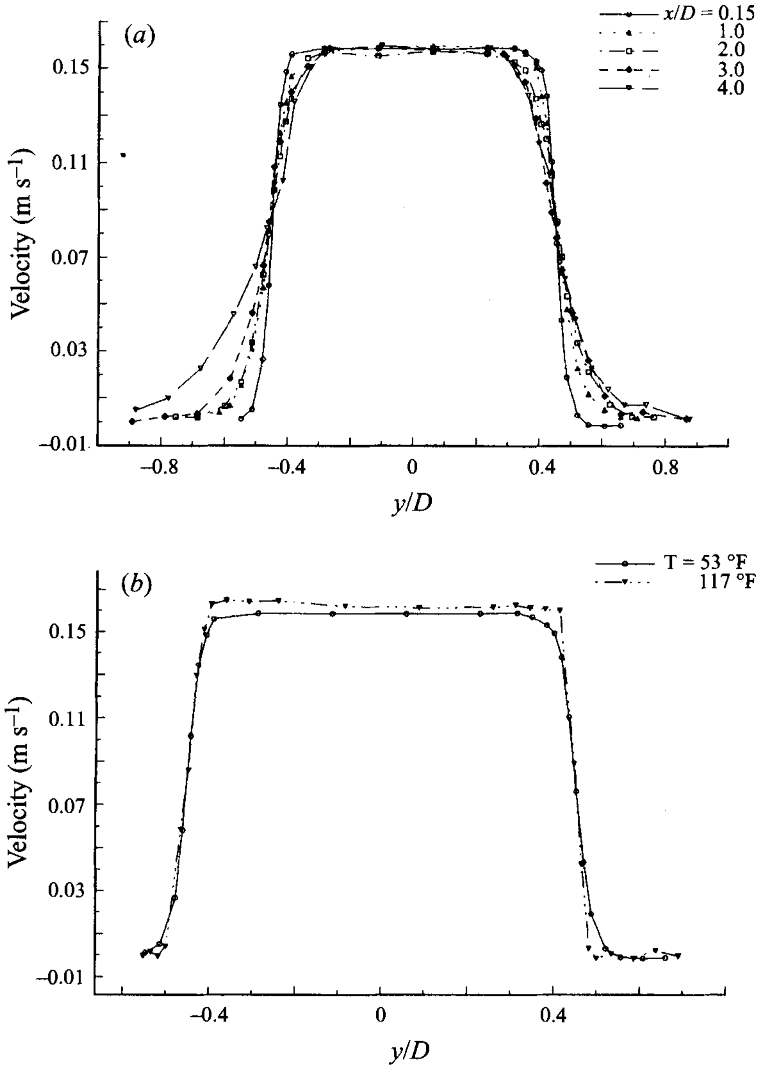

FIGURE 4. Streamwise velocity for spanwise traverses at the indicated x/D for a jet without tabs for (*a*) $Re = 1950$ only and (*b*) $Re = 1950$ and $R = 4160$.

D (cm)	T (°F)	$\nu \times 10^6$ ($m^2\ s^{-1}$)	U_{ref} ($m\ s^{-1}$)	Re_D	δ/D	θ/D ($x/D = 0$)	H	θ/D $x/D = 1$	$x/D = 2$	$x/D = 3$	$x/D = 4$
1.49	53	1.24	0.16	1950	0.049	0.0173	2.83	0.036	0.048	0.055	0.061
1.49	117	0.58	0.16	4160	0.039	0.0135	2.91				

TABLE 1. Water tunnel flow characteristics. Here D is the jet diameter, T the water temperature, ν the viscosity of the water, U_{ref} the centreline reference velocity, Re_D the Reynolds number, δ the mixing layer thickness, θ the momentum thickness, and H the shape factor

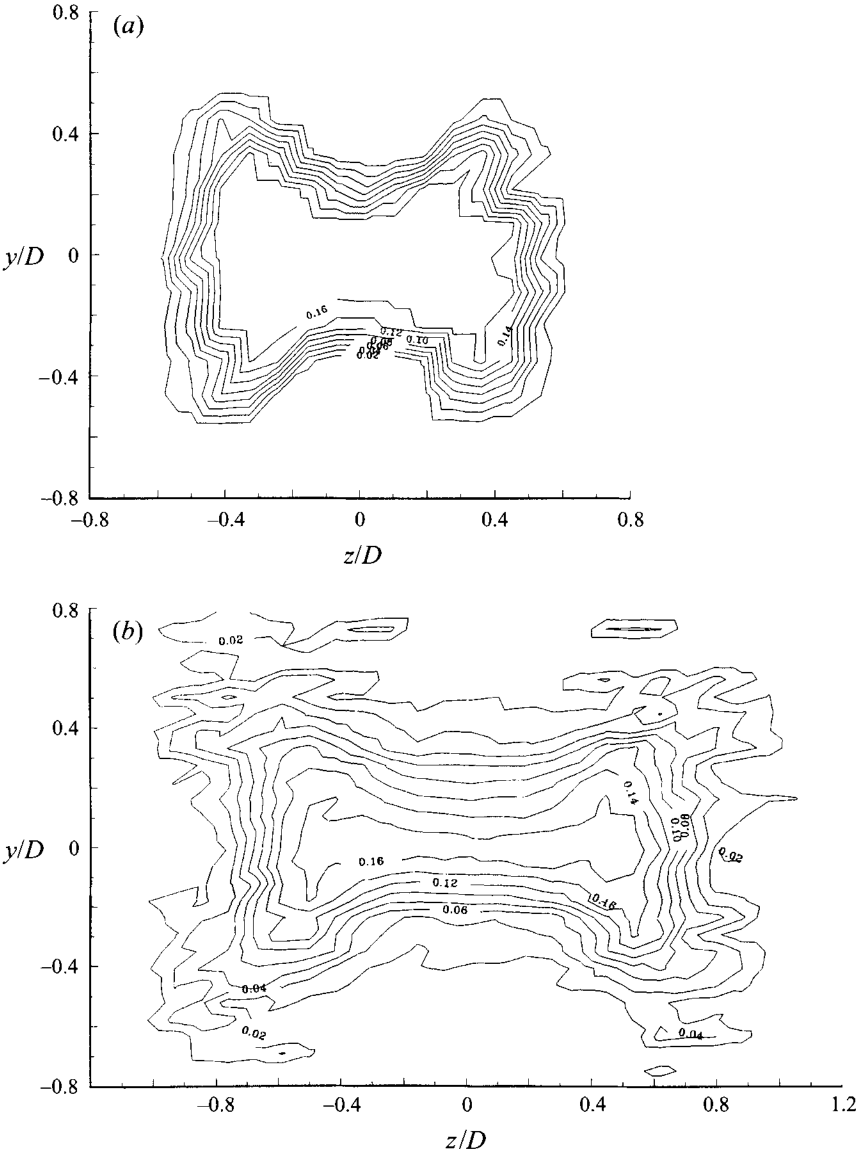

FIGURE 5. Streamwise velocity contours (in m s^{-1}) taken for a jet ($Re = 1950$) with two delta tabs at (*a*) $x/D = 0.5$ and (*b*) $x/D = 2.0$.

Because of the higher Reynolds number, the boundary layer, while remaining laminar ($H = 2.91$), becomes thinner. Table 1 contains information on the boundary layer for the high-temperature case as well.

When delta tabs are placed at the nozzle exit, the subsequent streamwise velocity pattern is markedly changed. Streamwise velocity contours taken at $x/D = 0.5$ and 2.0 are shown in figures 5(*a*) and 5(*b*), respectively. The upstream contours were derived from a 20×16 measurement grid (with $\Delta z = 0.114D$ and $\Delta y = 0.086D$) while the downstream values were obtained from a 32×26 grid (with $\Delta z = 0.057D$ and $\Delta y = 0.086D$). These detailed measurement grids were required because of the highly three-dimensional evolution of the jet. The splitting of the jet, seen in the time-averaged

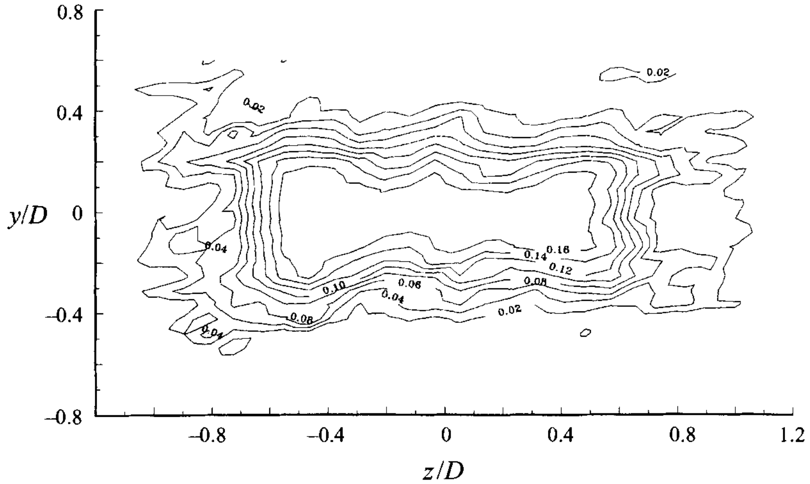

FIGURE 6. Streamwise velocity contours (in m s^{-1}) taken at $x/D = 2.0$ for a jet ($Re = 1950$) with two inverted delta tabs.

flow visualizations (figure 3(*b*), is even more apparent here. The thickness of the mixing layer increases with downstream distance as expected. The layer appears to grow more quickly along the axis of the tabs than along the axis normal to the tab placement.

Streamwise velocity measurements where inverted delta tabs are used to perturb the jet are shown in figure 6. As for the delta tab case, this cross-section was taken at $x/D = 2$ using the same grid resolution. The contour shape follows the visualization of figure 3(*d*) in that the jet core is longer in the z-direction compared to the delta tab case. The small ejection of core fluid at the tip of each tab is apparent in this data.

3.3. *Mean secondary velocity results*

Measurements of the secondary flow in the water tunnel were obtained from the two-component LDV measurements. Ideally, the V- and W-components of velocity could have been measured simultaneously. However, access to the tunnel was difficult. Therefore, the following results were obtained by measuring one secondary flow component (e.g. V) at a time along with the streamwise component, U. Then, instead of moving the fibreoptic probe to a different location (which would have required both recalibration of the probe and adjustments to the traversing system), the tabs themselves were rotated about the nozzle axis. This did introduce very slight variations in the tab placement, but was found to be an adequate means of measuring the secondary flows generated by the tabs.

The mean secondary velocity components measured at $x/D = 0.5$ with two delta tabs in place are shown in figure 7. For these and subsequent figures, the tab axis corresponds to the y-axis. The solid contours represent positive values for the indicated quantity, and dashed lines indicate negative values. It can be clearly seen in figure 7(*a*) that the tabs produce a nearly symmetric secondary flow, W (hereafter referred to as the lateral component of velocity), away from the tab axis. The maximum contour levels of 0.020 m s^{-1} for W are approximately 1/8 the value of the streamwise velocity in the jet core (0.16 m s^{-1}). Notice that the maximum levels occur in four regions on both sides of each tab. The secondary flow component parallel to tab axis, V (hereafter referred to as the spanwise velocity component), is shown in figure 7(*b*) for the $x/D = 0.5$ location. From this plot it is clear that the tabs pump fluid into the jet core

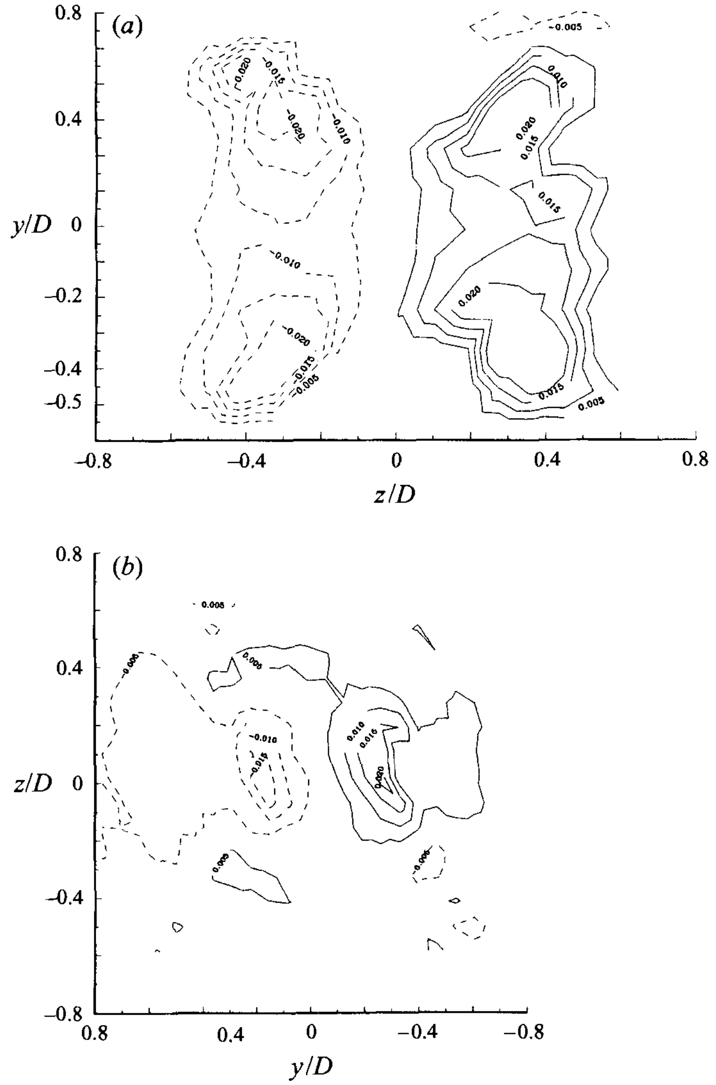

FIGURE 7. (*a*) Lateral (W) and (*b*) spanwise (V) velocity component contours at $x/D = 0.5$ for the jet ($Re = 1950$) with two delta tabs. The tabs were positioned on the y-axis (at $z/D = 0$).

along the tab axis. The contour levels are slightly lower for V than for W but are still well above background noise levels.

The same mean velocity components for the same tab configuration were measured at $x/D = 2$ and are shown in figure 8. The lateral velocity (W) shown in figure 8(*a*) maintains its symmetric features, and the maximum contour levels drop only slightly compared to the $x/D = 0.5$ data. The spanwise component (V), shown in figure 8(*b*), does appear to drop somewhat more between x/D of 0.5 and 2.0. Just as at $x/D = 0.5$, the two-delta-tab configuration pumps fluid away from the axis of the tabs (spanwise axis) and toward the jet centre along the tab axis.

From these sets of velocity data, it is clear that each tab generates a strong pair of counter-rotating streamwise vortices which deform the flow. The streamwise vorticity ($\partial W/\partial y - \partial V/\partial z$) normalized by U_{ref}/D was directly calculated for the $x/D = 0.5$ case

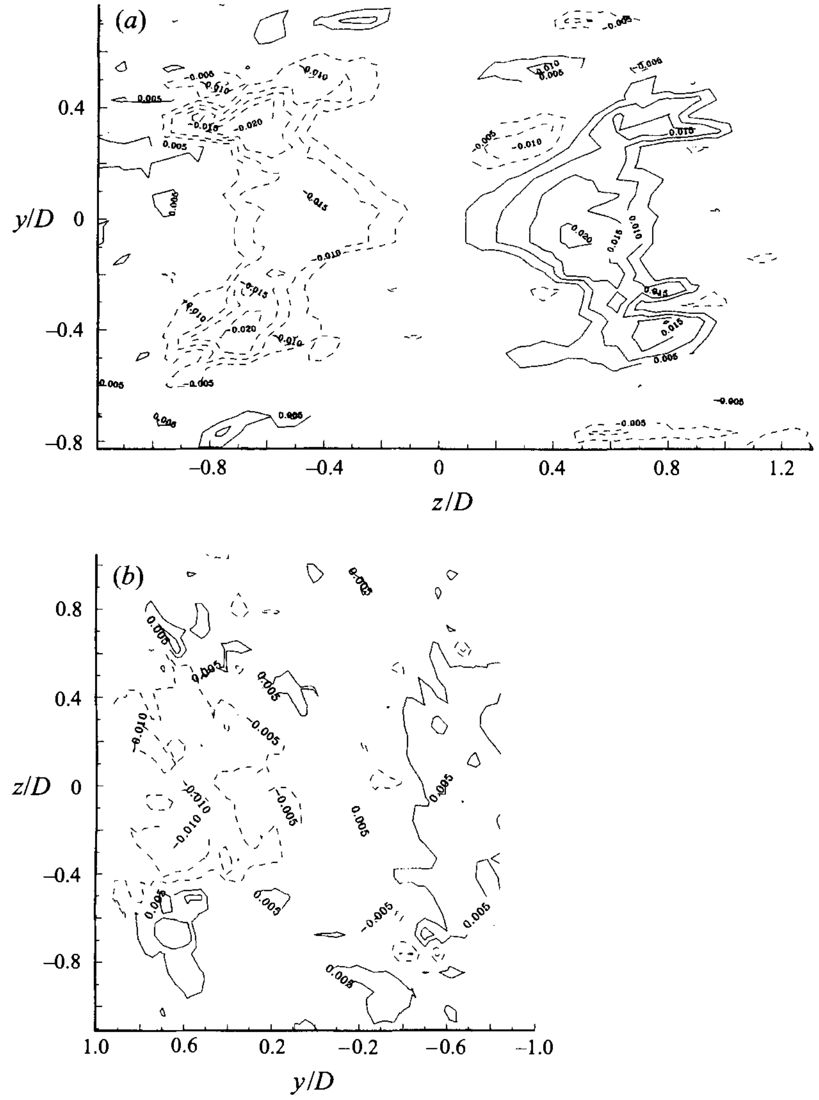

FIGURE 8. (*a*) Lateral (W) and (*b*) spanwise (V) velocity component contours at $x/D = 2.0$ for a jet ($Re = 1950$) with two delta tabs. The tabs were positioned on the y-axis (at $z/D = 0$).

and is shown in figure 9. As with the streamwise velocity measurements, the spatial resolution of the grid used for these cases is approximately $0.1D$ by $0.1D$. The four large vortices shown circulate such that fluid is entrained along the axis of the tabs.

In addition to the stronger vortices which cause the bifurcation of the jet, the tabs generate two additional, weaker vortices just outside the stronger ones. These are indicated by the arrows in figure 9. The rotation and location of these secondary vortices are consistent with that of the legs of the 'horseshoe' vortex which forms on a boundary layer with a protuberance. These are also shown clearly in flow visualizations given in the next section. It seems reasonable to conclude that these vortices are in fact the legs of the horseshoe vortex, which is generated by the wrapping of the boundary layer around the tabs. Although it is possible that the secondary vortices form due to 'spinning off' the primary streamwise vortices, their appearance

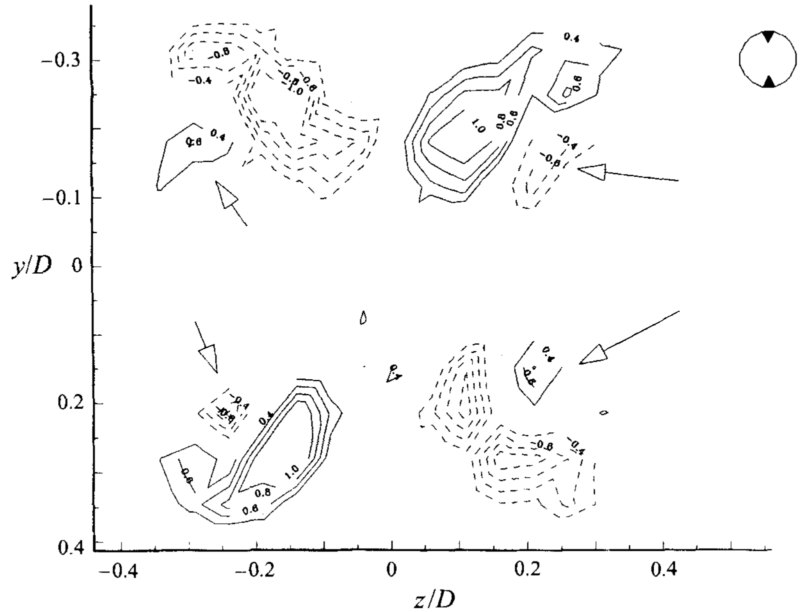

FIGURE 9. Streamwise vorticity contours at $x/D = 0.5$ for a jet ($Re = 1950$) with two delta tabs. The tabs were located on the y-axis (at $z/D = 0$). Horseshoe vortices are indicated by the arrows.

at this upstream location makes that hypothesis highly unlikely. The horseshoe vortices do appear to persist at the $x/D = 2$ location as well. This is indicated by the outward jettison of fluid in the W-component measurements of figure 8(*a*).

When inverted delta tabs are used to perturb the flow, the secondary flow patterns become even more complex. The secondary flow components at $x/D = 2$ are shown in figure 10. The overall velocity features of the inverted delta tab case are similar to the delta tab case. In addition to the stronger vortices which bifurcate the jet and the weaker horseshoe vortices which occur due to the wrapping of the boundary layer, the flow visualizations and the streamwise velocity measurements indicate another pair of weak vortices which form at the tab tip. The magnitude of these vortices is too small to be quantified here with the grid resolution used. Their presence may be recognized to a degree by considering the V-component contours of figure 10(*b*), but the levels are hardly distinguishable from noise. Instantaneous flow visualizations to be presented better show these 'tip' vortices.

The overall pattern of streamwise vortices generated by delta and inverted delta tabs for these incompressible jet experiments is sketched in figures 11(*a*) and 11(*b*), respectively. Each delta tab generates a pair of strong streamwise vortices which act to bifurcate the jet, as well as a pair of weaker vortices which are the legs of the horseshoe vortex. Each inverted delta tab produces three sets of counter-rotating vortices. In addition to the two sets generated by each delta tab, there is a weak pair of vortices which form close to the tip of each tab which act to pump fluid away from the jet core along the axis of the tabs.

3.4. *Instantaneous flow visualizations of the tab effect*

Flow visualizations were obtained not only for time-averaged cases presented earlier, but also for instantaneous images. While the time-averaged images show quite nicely the overall effect of the tabs, the instantaneous visualizations yield additional insight

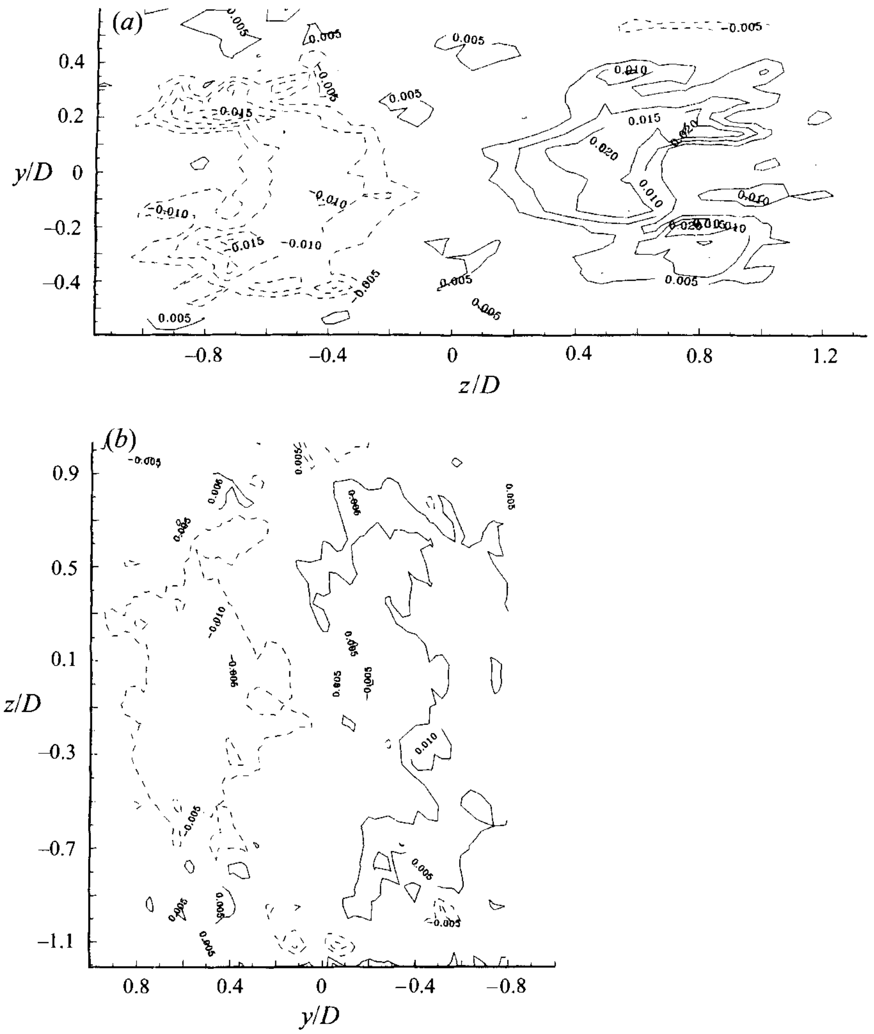

FIGURE 10. (*a*) Lateral (W) and (*b*) spanwise (V) velocity component contours at $x/D = 2.0$ for a jet ($Re = 1950$) with two inverted delta tabs. The tabs were positioned on the y-axis (at $z/D = 0$).

into the finer properties of the flow. Owing to the low velocity of the flow, it was possible to capture these visualizations in real time.

3.4.1. *Single view images of the jet*

The instantaneous visualizations for the water tunnel were obtained using ordinary video cameras as described earlier. The frame rate, which yielded 60 image fields per second, was fast enough to capture the temporal evolution of structures within the jet. The images presented in this subsection were recorded with a single camera positioned to capture either a front view or a side view of the jet.

Figure 12 shows single images of a front view (*a*) and a side view (*b*) of the natural jet where the core is seeded with fluorescein. The side view extends from the nozzle exit to approximately two jet diameters downstream and the flow is moving left to right. As shown in the corresponding sketch, the side-view laser sheet passes vertically through the jet axis. There appears to be no Kelvin–Helmholtz (K–H) roll-up by

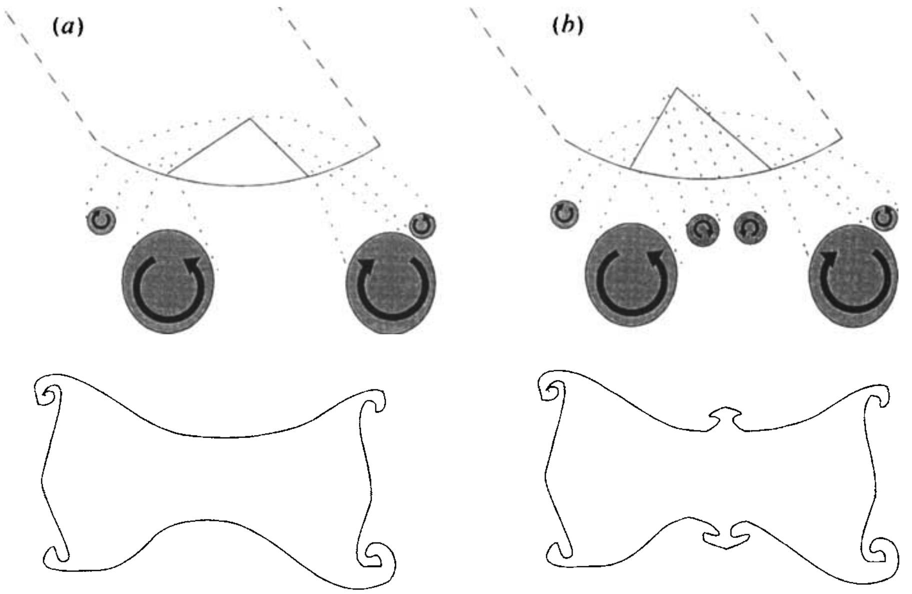

FIGURE 11. Sketch of the streamwise vorticity patterns generated about a single tab (top) and the resultant jet deformation due to two tabs (bottom) for (*a*) delta tabs and (*b*) inverted delta tabs.

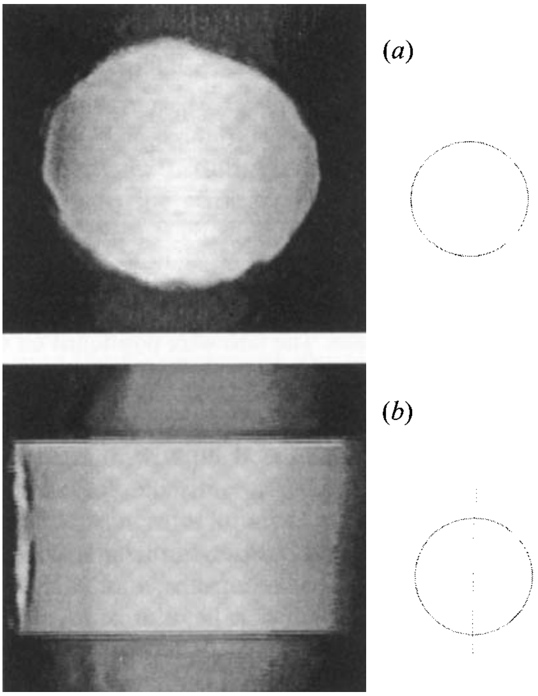

FIGURE 12. Instantaneous views of an incompressible ($Re = 1950$) jet without tabs: (*a*) a front view at $x/D = 0.5$ and (*b*) a side view from approximately $x/D = 0$ to 2 with the flow moving left to right. The accompanying sketches indicate the plane of the laser sheet.

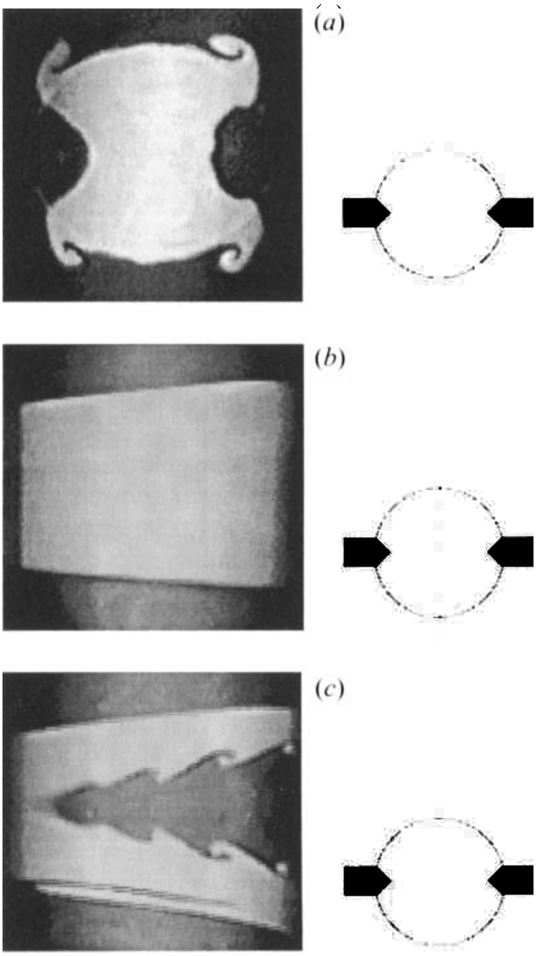

FIGURE 13. Views of an incompressible ($Re = 1950$) jet with two delta tabs: (*a*) a front view at $x/D = 0.5$, (*b*) a side view from approximately $x/D = 0$ to 2 through the centre of the jet, and (*c*) a side view taken along a plane near a tab tip. The sketches indicate the laser sheet and tab positions.

$x/D = 2$. The front view taken at $x/D = 0.5$ simply shows the circular region of the jet core. The small non-uniformities around the circumference of the jet are likely due to very fine irregularities at the jet exit.

Images for the same flow conditions were taken for a jet with two delta tabs oriented as shown in figure 13. The dramatic effect of the tabs is made apparent once again in these images. The front view shows the bifurcation of the jet core region. Perhaps the most dramatic feature of these images are the four outermost sectors of the jet where the core fluid appears to swirl into streamwise vortices. Note that these vortices are not the 'strong' vortices which act to bifurcate the jet but are instead the legs of the weaker horseshoe vortices. This observation is consistent with the streamwise vorticity measurements of figure 9.

In figure 13, two side views are shown in (*b*) and (*c*) corresponding to variations in the spanwise location of the laser sheet. The view in (*b*) corresponds directly to the natural jet image of figure 12(*b*) where the sheet passes through the jet along its centreline. There are two points of interest in this image: (i) there does not appear to

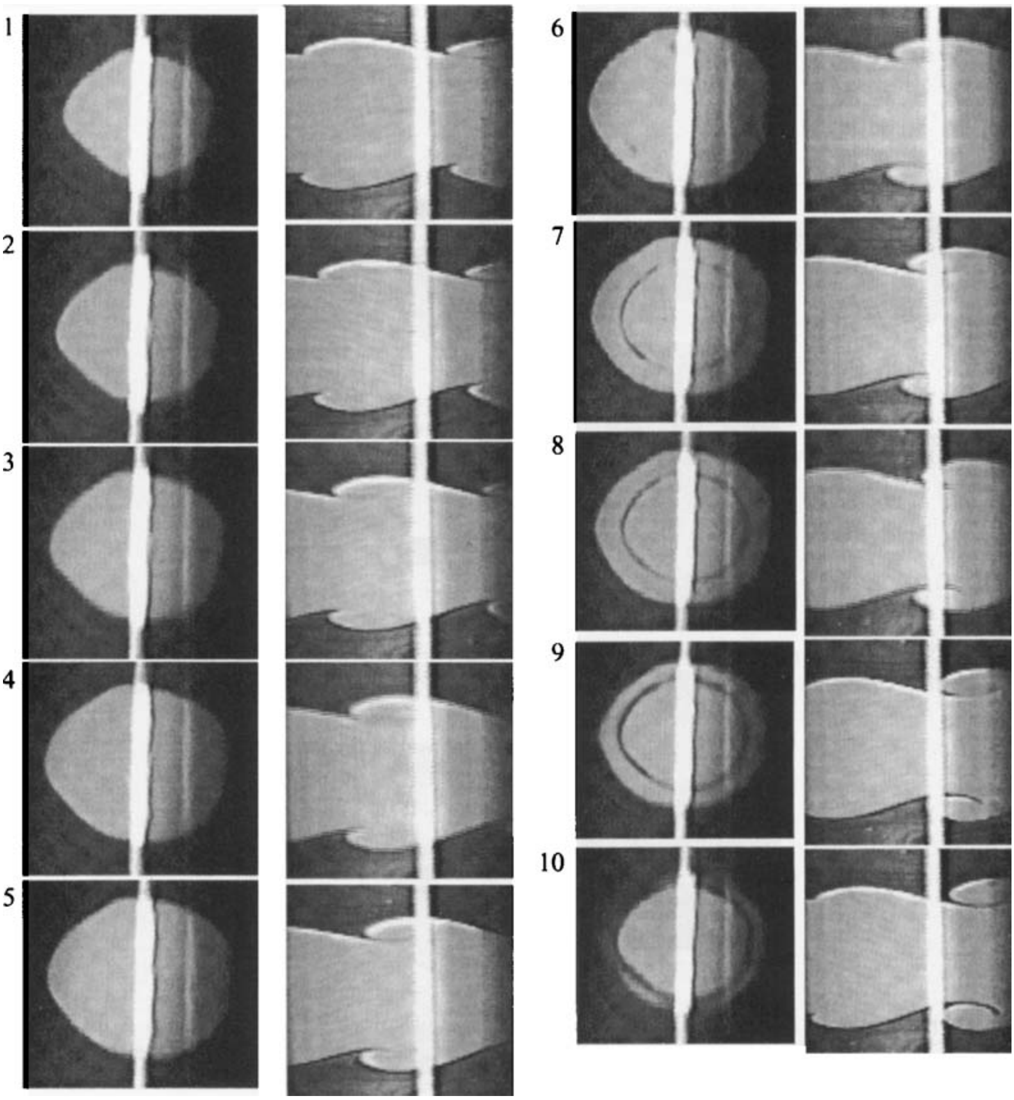

FIGURE 14. Dual-view real-time simultaneous visualizations of a jet ($Re = 1950$) without tabs. The left column is a front view at $x/D = 3$. The right column is a side view ($x/D = 2$ to 3.5) with the flow moving left to right and the laser sheet passing through the centreline. Frame numbers (1–10) at the upper left indicate progression in time.

be any K–H roll-up; and (ii) the angle at which the jet spreads in this plane has increased compared to the no-tab case. The side view with the laser sheet passing in the vicinity of a tab tip is given in (*c*). Here, it can be seen that the tabs not only influence the average features of the flow but also change aspects of time-dependent quantities. In the vicinity of the tab tip, the K–H roll-up occurs much further upstream. The roll-up occurs on either side of the tab in a symmetric pattern. As these K–H structures convect downstream, they develop more well-defined features as they grow. There are two reasons why the structures develop much further upstream for this spanwise location. The first is that the effective radial curvature is sharply increased very near the tabs. The second is that a tab acts to thin the boundary layer on its own surface. The dark thin area at the lower part of this image represents ambient fluid at the core of a horseshoe vortex. This is not seen in the top part of the image, possibly due to a slight lateral angle in the laser sheet.

3.4.2. *Real-time dual-view images of the jet*

Since the tabs produce such highly three-dimensional perturbations to the flow, single-plane visualizations tell only part of the story. To remedy this, a unique approach to the visualizations was taken. Two cameras were used to record two normal planar images of the flow. The cameras could be synchronized from tape review, and thus yielded simultaneous real-time dual-view visualizations.

Figure 14 shows a progression of simultaneous front (on the left) and side views (on the right) of a natural jet with a Reynolds number of 1950 at the jet exit. The frame numbers appear to the left of each front view image and correspond to both front and side views for each row. The bright vertical line in each image is the laser sheet for the alternate view. While this bright line due to the normal laser sheet obscures some flow features, it is useful in determining the exact locations of the visualizations. In some front view pictures a faint second vertical line due to a reflection from the free surface is visible to the right of the bright line. This reflection should not be mistaken for a feature of the flow. The front-view sheet is located at $x/D = 3$ where the vortex rings are beginning to roll up. The jet is basically axisymmetric at this point with just a few azimuthal irregularities. From the side-view images of figure 14, the formation and passage of a vortex ring can be followed in time. The initial 'bump' of core fluid on the far left of the first side view image grows throughout the progression of images and convects downstream (with the flow moving left to right). In this side view, which extends from about $x/D = 2$ to 3.5, it can be seen that a vortex ring passes in about nine or ten image fields. This leads to a convection velocity of roughly 8–9 cm s^{-1} (0.5–$0.6U_{ref}$). While this value of U_c should be taken as nominal since only one structure passage is considered, it is consistent with expected values.

The front-view images of figure 14, which were taken at $x/D = 3$, likewise show the evolution of this ring structure. These images in the left column correspond to the same instant in time (at least within half a frame) as the side view images in the same row. The apparent jet diameter, where the fluorescein-laden fluid is present, increases steadily in frames 1–5. By frame 6, faint dark areas of entrained ambient fluid appear. By frames 8 and 9 the entrained fluid definitely takes a ring-like shape, demonstrating the K–H roll-up quite nicely. By frame 10, of both the front and side views the ring has passed and a new cycle is beginning.

Dual-view images using a similar set-up were taken for the two-delta-tab case, and are shown in figure 15. In these images the front view was taken at $x/D = 2$ (instead of $x/D = 3$ for the no-tab case). In the side views of figure 15, nearly symmetric vortex rings are seen to roll up and convect downstream (left to right). With the laser sheet for this view located along the jet centreline, the roll-up of vortices appears similar in many ways to that of a natural jet. The front-view images are staggered in order to save space while magnifying details of the mixing.

The front view, in the left-hand columns of figure 15, show some remarkable features of the evolution of this jet. The spanwise extent (horizontal axis, as shown) of the fluorescein-laden fluid practically doubles from frame 1 to frame 4. By the fifth frame, interwoven layers of ambient and core fluid appear on either side of the jet centre. (Note that these layers are more fully formed at $x/D = 2$ for the delta tab case than at $x/D = 3$ for the natural jet.) Frame 6 of this sequence perhaps best shows the intricate details of the mixing. Three layers of ambient fluid are visible on either side

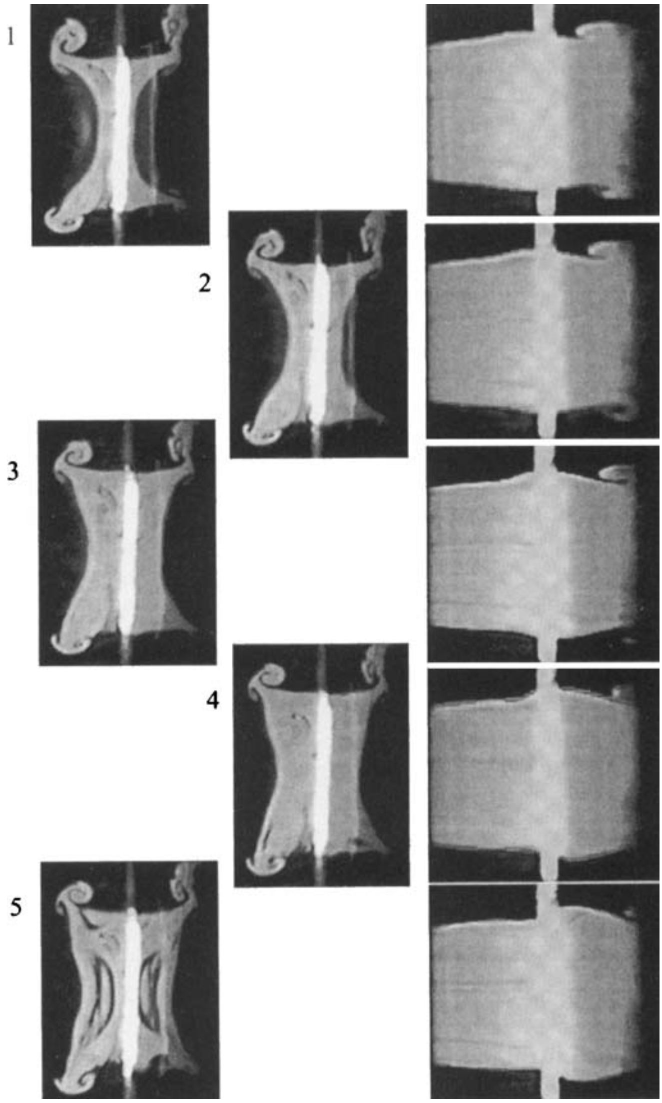

FIGURE 15(1–5). For caption see facing page.

of the jet centre. It is notable that this image corresponds to the side-view images just after the K–H roll-up passes by the front-view laser sheet. In frames 7–10, the ambient layers grow smaller, and by frame 10 a full cycle has essentially been completed. Prominent in each of these frames are the horseshoe vortices at the outermost regions, which were also noted in figure 12(*a*).

The details of the mixing were further illuminated when the side-view laser sheet was positioned close to a tab tip rather than the jet centreline. These images are shown in figure 16. This set of images was chosen such that the progression of front-view images matches that of figure 15 relatively well. The finer features of the mixing patterns induced by the tab effect are evident here. The strong streamwise vortices generated by the tabs interact with the vortex rings to produce vivid images of a periodic highly three-dimensional mixing layer at $x/D = 2$. The emergence of layers of ambient and

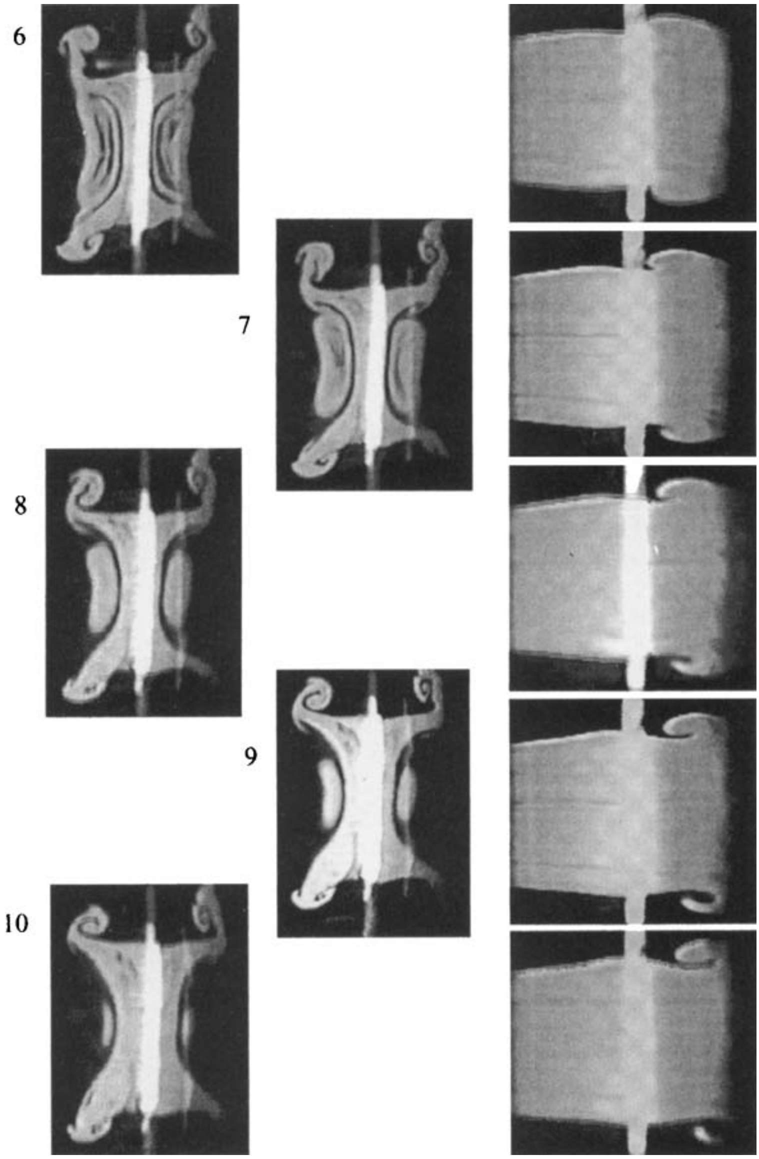

FIGURE 15. Dual-view real-time simultaneous visualizations of a jet ($Re = 1950$) with two delta tabs. The left column is a front view at $x/D = 2$. The right column is a side view ($x/D = 1$ to 3). Otherwise, as figure 14.

core fluid can be seen in the front views of frames 5–8 although the left half of the images is partially obscured by the side-view laser sheet. Again, the ten images show approximately one vortex roll-up cycle.

In the side view of figure 16, it can once again be seen that the tabs split the jet. This can be observed by noting the top and bottom of each frame where the flow consistently appears bright. Between these two regions, intermittent areas of fluorescein-laden flow 'bridge' the two core regions. These bridges generally appear to be swept upstream in the centre of this visualized plane.

Upon closer examination, a great deal can be learned from the evolution of one such

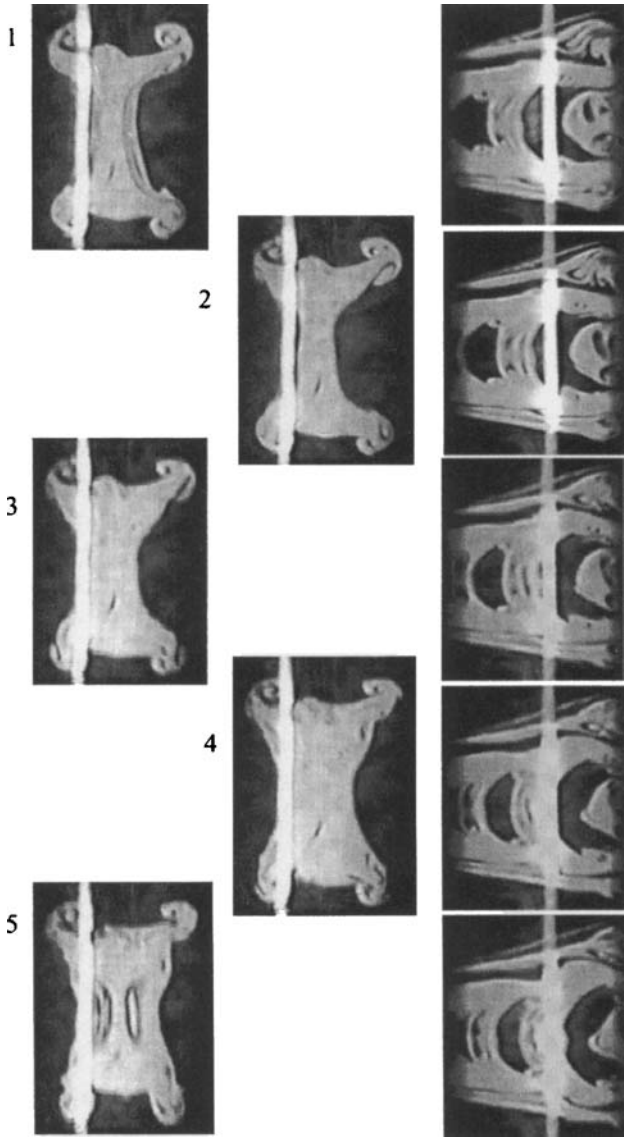

FIGURE 16(1–5). For caption see facing page.

structure visible in this side-view sequence. Beginning with frame 1, there is a bright structure present at the far left with two dark 'eyes' situated very close to each bright stream. This particular feature can be seen to spread out laterally as it convects downstream. Within the first five frames, the convecting structure can clearly be seen to contain layers of ambient fluid. The passage of this structure through the front-view sheet corresponds to the layered mixing region of the jet seen in the front view (frames 6–8). By frames 9 and 10, the bulk of the bright structure has passed the front-view sheet and has become more developed. The two eye-shaped regions have engulfed more ambient fluid and show greater detail at this downstream location. Meanwhile, another structure with very similar characteristics can be seen developing at locations upstream in frames 7–10.

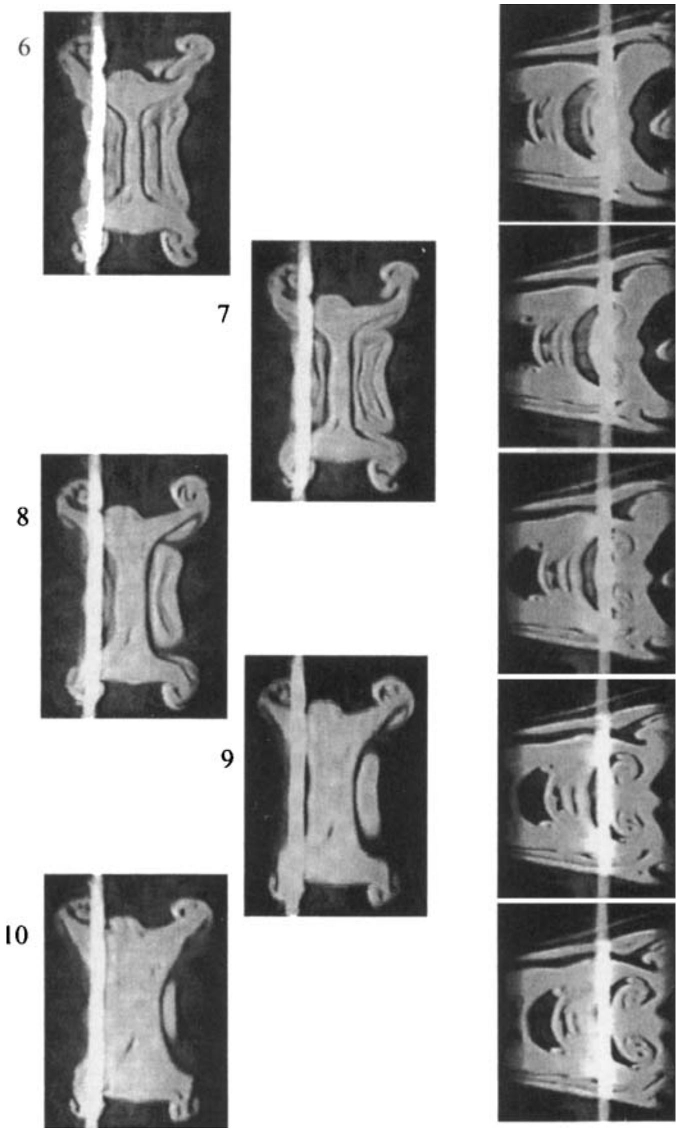

FIGURE 16. As figure 15 but the side-view laser sheet was positioned close to a tab tip.

The dual-view instantaneous visualizations for the inverted delta tab cases are given in figure 17. As for the previously discussed tab cases, these were performed for $Re_D = 1950$ with the front-view laser sheet at $x/D = 2$. The side-view sheet was located somewhat further upstream for these cases (approximately 1 to 2.5). The progression of images was kept fairly consistent with the delta tab cases presented earlier. Many features of the jet with inverted tabs are similar in nature to the other tab cases, but there are some additional details.

The front view images leave no doubt that two counter-rotating vortices are present at each tip and act to eject core fluid away from the jet centreline. The ejection is notable in each of the front-view frames. In some frames, the seeded fluid can be seen to swirl in the direction of the vortices much as the horseshoe vortices do. As with the delta tab case, when a large-scale structure passes the front sheet, layers of core and

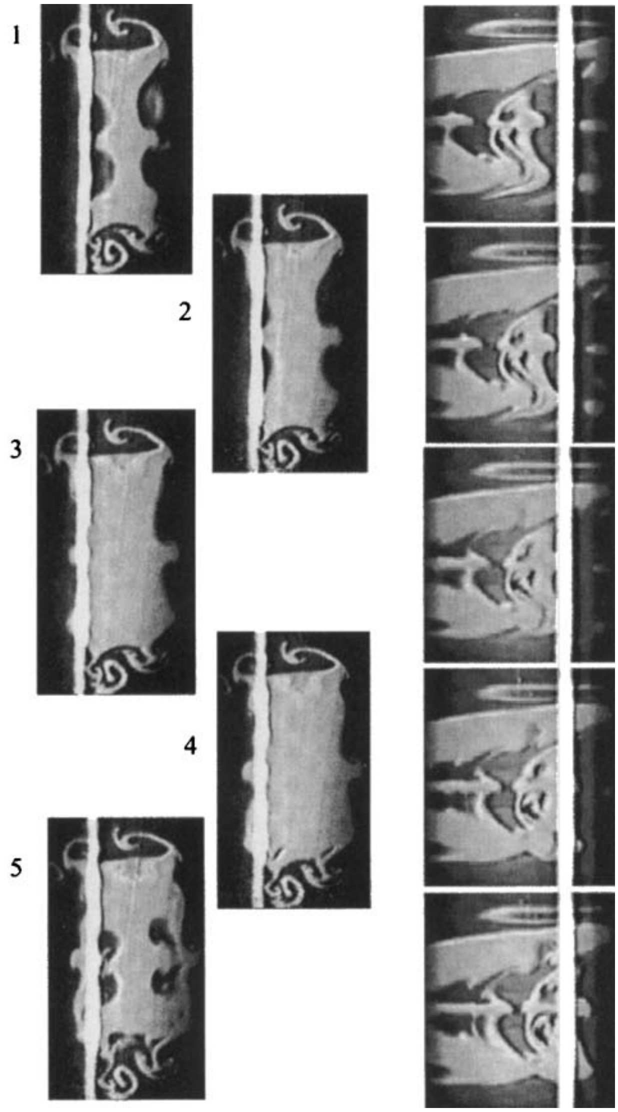

FIGURE 17(1–5). For caption see facing page.

ambient fluid are formed in the mixing region near the tabs. This occurs in frames 5–8 of this sequence. It is notable that for this inverted delta tab case, the layers are broken by the ejection from the jet core. This is particularly evident in frames 7 and 8 of the front view. Once again, horseshoe vortices are present at the very top and bottom of each frame.

Overall, the side-view images of figure 17 are similar in nature to the delta tab case, except for a streak of fluorescein-seeded fluid present along the centre of the plane visualized that was not present for the delta tab case. This is simply due to the ejection of core fluid near the tab tip. While the vortices causing the ejection are not very strong, their presence dramatically influences the visualization of this particular plane. Once again the evolution of structures can be followed in time, and it is clear that the convection velocity of these structures is similar to that seen previously. Owing to

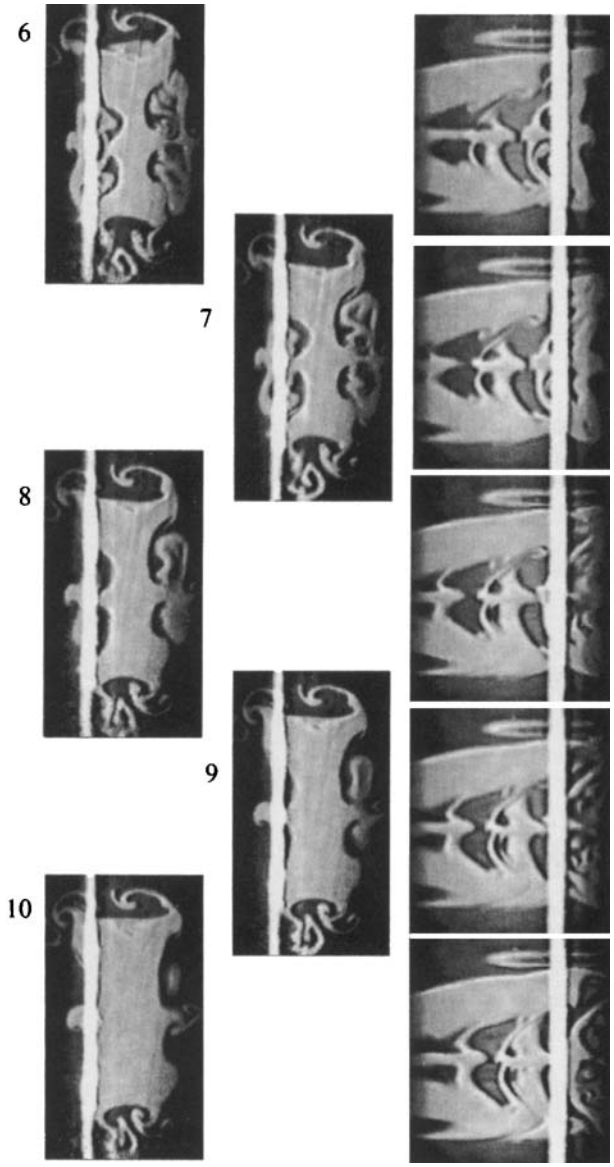

FIGURE 17. Dual-view real-time visualizations of a jet ($Re = 1950$) with two inverted delta tabs. The left column is a front view at $x/D = 2$. The right column is a side view ($x/D = 1$ to 2.5) with the flow moving left to right and the laser sheet passing near a tab tip.

a slight angle of the laser sheet the horseshoe vortex at the top but not the bottom is seen – of course, the presence of both is clear from the front view images.

One set of dual-view images was performed for a delta tab case where the Reynolds number was increased to 4160. These visualizations are shown in figure 18. As described in §2, this was accomplished without varying either the jet diameter or the flow rate. Instead, the temperature of the water was increased from 53 °F to 117 °F. This enables direct comparison of the evolution of structures, which convect at approximately the same velocity as seen in figures 15 and 16. The temperature of the ambient water was also raised to 117 °F to eliminate density effects and to enable

FIGURE 18(1–5). For caption see facing page.

focusing of the front-view camera. These $Re = 4160$ cases were taken with the front-view sheet at $x/D = 2$ and with the side view sheet extending from about $x/D = 1$ to 2.5. Boundary layer characteristics for this Reynolds number jet (no tab) are given in table 1.

In comparing figures 16 and 18 it is clear that essentially doubling the Reynolds number from 1950 to 4160 has a tremendous effect on the organization of the mixing layer. The front views of the $Re_D = 4160$ case are not nearly as symmetric as the $Re_D = 1950$ case, and both views exhibit smaller-scale structures than figure 16. The side view shows that the K–H structures roll up into identifiable vortices much further upstream. In frame 1 of the side view, two vortices can be seen entraining ambient fluid toward the centre of the visualized plane even at roughly $x/D = 1$. These vortices may

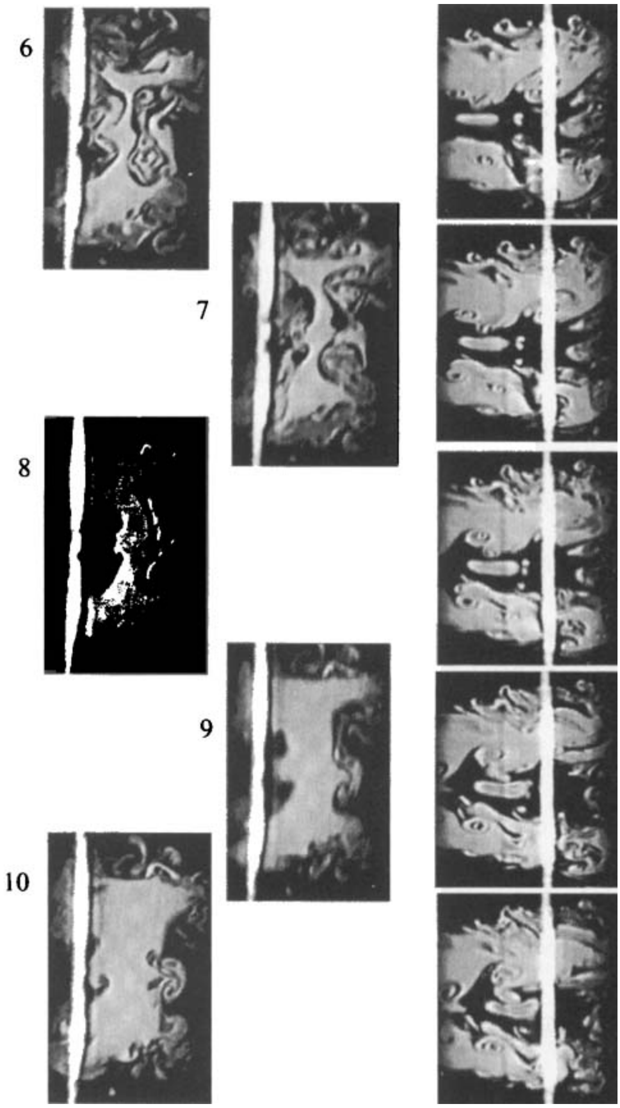

FIGURE 18. Dual-view real-time simultaneous visualizations of a jet with the same views and tab configuration as figure 16, but for a jet with a higher turbulence level ($Re = 4160$).

be tracked in frames 2–5, but become highly disorganized by frames 6 and 7. By frame 8 a new pair of vortices roughly at $x/D = 1$ can be seen to emerge and convect downstream in a similar manner in frames 9 and 10.

It is noteworthy that while the overall effect of the tabs (i.e. bifurcating the jet) is evident in the $Re_D = 4160$ case, there are subtle differences. For example, the horseshoe vortices are less obvious in these visualization. This is partly due to the thinner boundary layer (see table 1). From the front view, one can see that the seeded area within the core of the jet expands and contracts much like the $Re_D = 1950$ case. However, the frequency of these fluctuations is not as clearly defined for the higher Reynolds number case. This matter was further explored using spectral measurements with LDV and is discussed next.

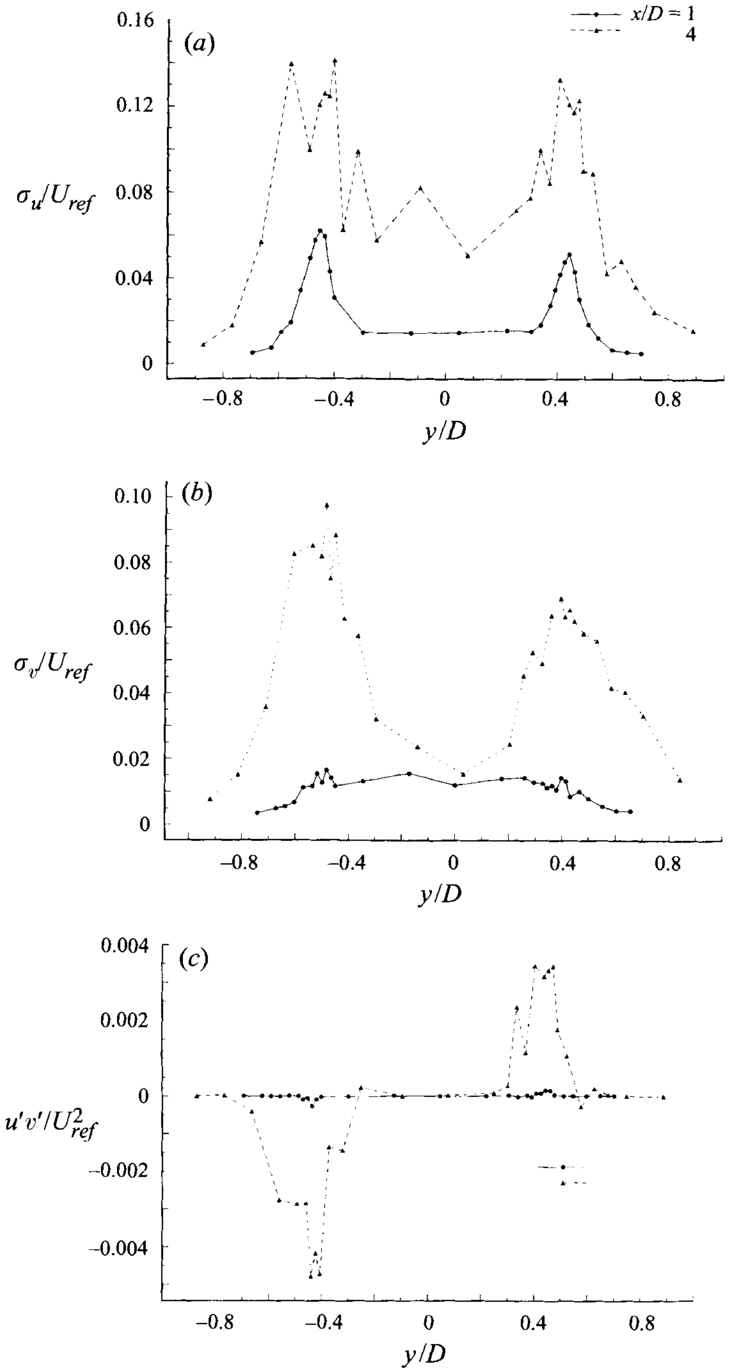

FIGURE 19. (*a*) Streamwise normal Reynolds stress σ_u, (*b*) spanwise (also radial) normal Reynolds stress σ_v, and (*c*) Reynolds shear stress $\overline{u'v'}$ for a jet ($Re = 1950$) without tabs at the indicated locations.

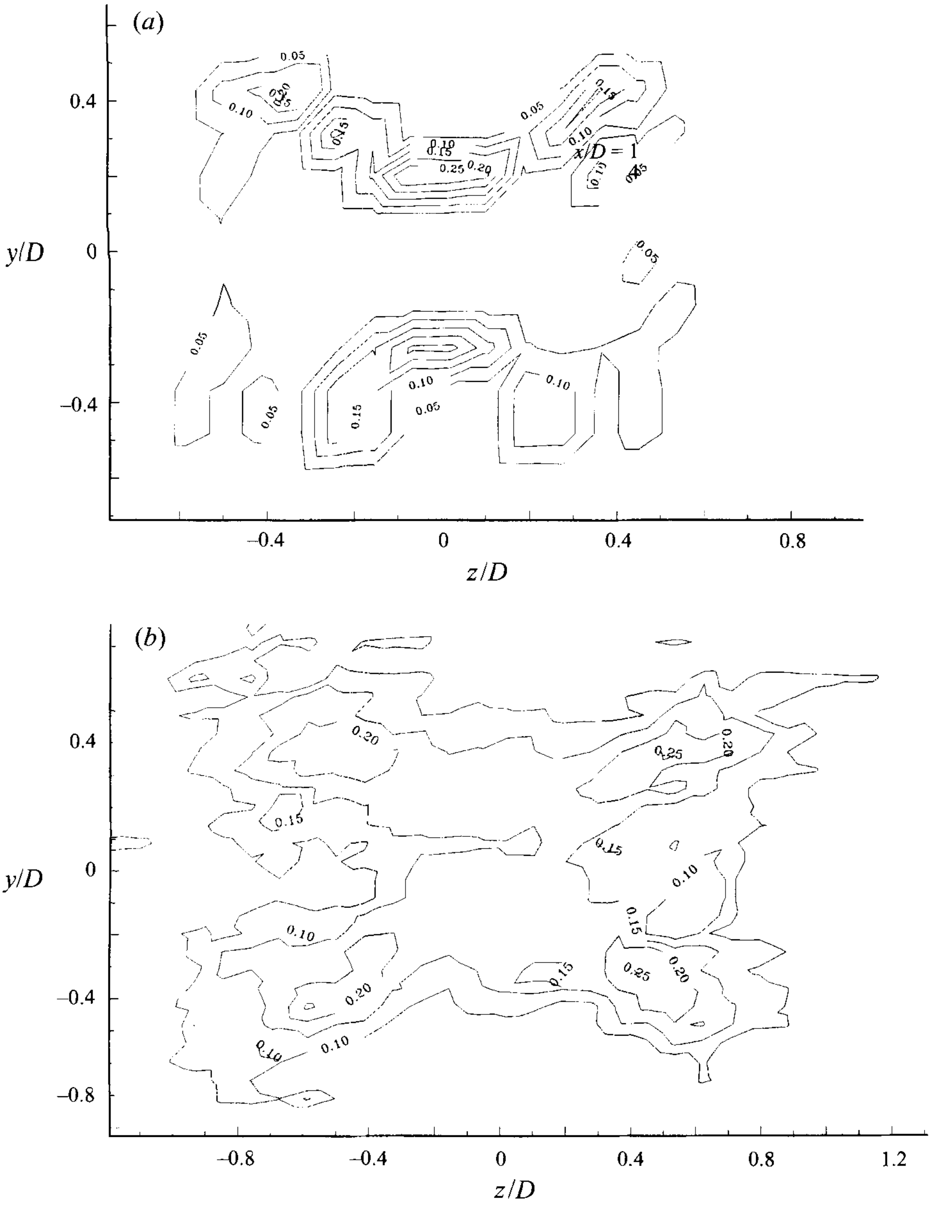

FIGURE 20. Streamwise normal Reynolds stress, σ_u, contours for the two-delta-tab case (with the tabs along the y-axis) taken at (a) $x/D = 0.5$ and (b) $x/D = 2$. All data here and in subsequent figures are normalized by U_{ref} ($= 0.16$ m s^{-1}).

3.5. *Turbulence characteristics of the jets*

In addition to varying the mean quantities of the flow, it is clear from the instantaneous visualizations of §3.4 that temporal characteristics are also altered by the tabs. Reynolds normal and shear stresses (normalized using the centreline velocity of 0.16 m s^{-1}) were calculated for various cases. The data rate for the incompressible jet LDV measurements was sufficient to gather spectral characteristics of the flow, and these revealed some particularly interesting results.

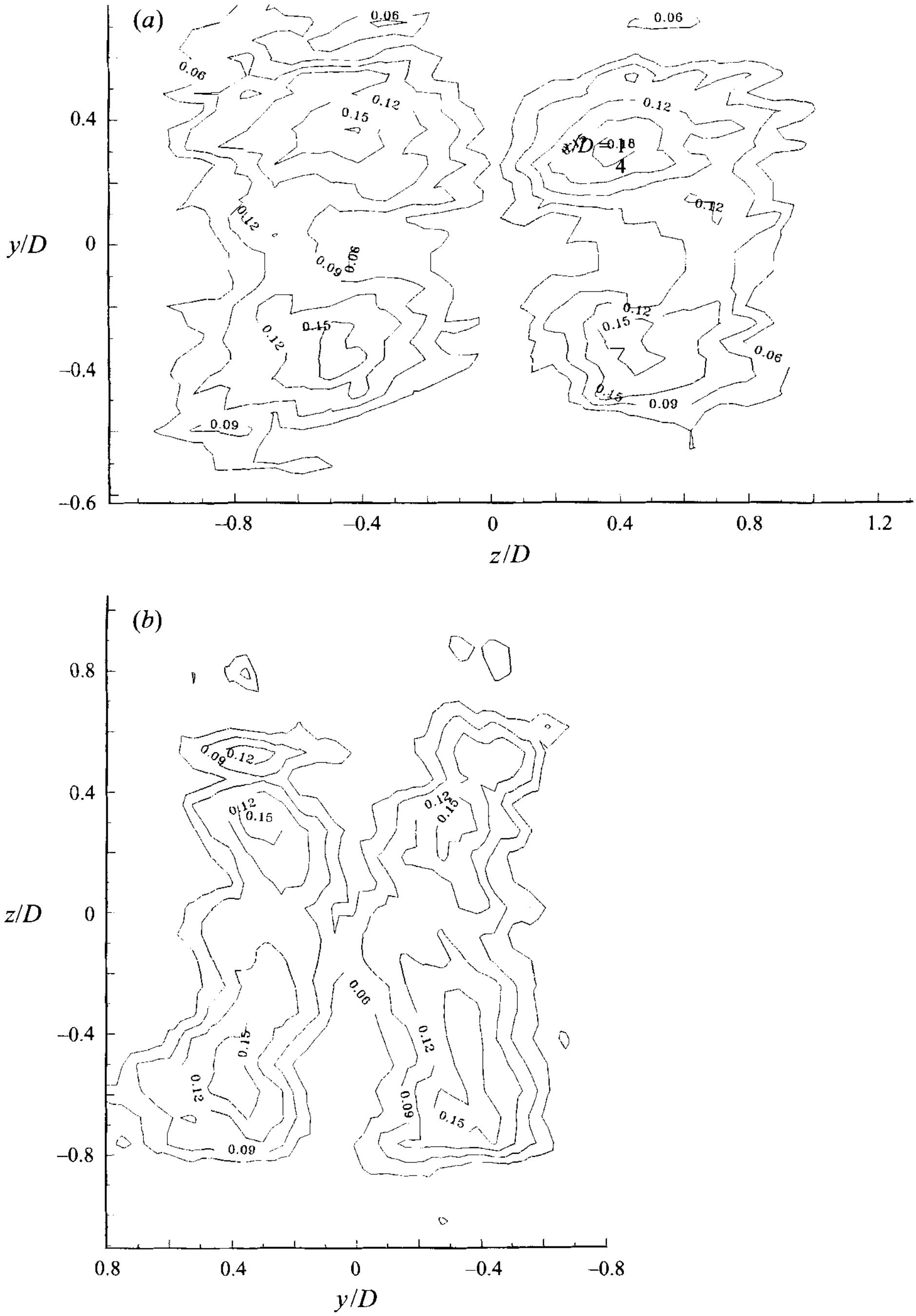

FIGURE 21. Contours of (*a*) lateral normal Reynolds stress, σ_w, and (*b*) spanwise normal Reynolds stress, σ_v, for the two-delta-tab case at $x/D = 2$.

3.5.1. *Reynolds stress results*

Streamwise normal Reynolds stress, σ_u/U_{ref}, values for two spanwise traverses through a jet without tabs are given in figure 19(*a*). For reference, the mean velocity was given earlier for the same traverses in figure 3. The peak fluctuations occur within the mixing layer, as one would expect. The overall magnitude of the fluctuations rose

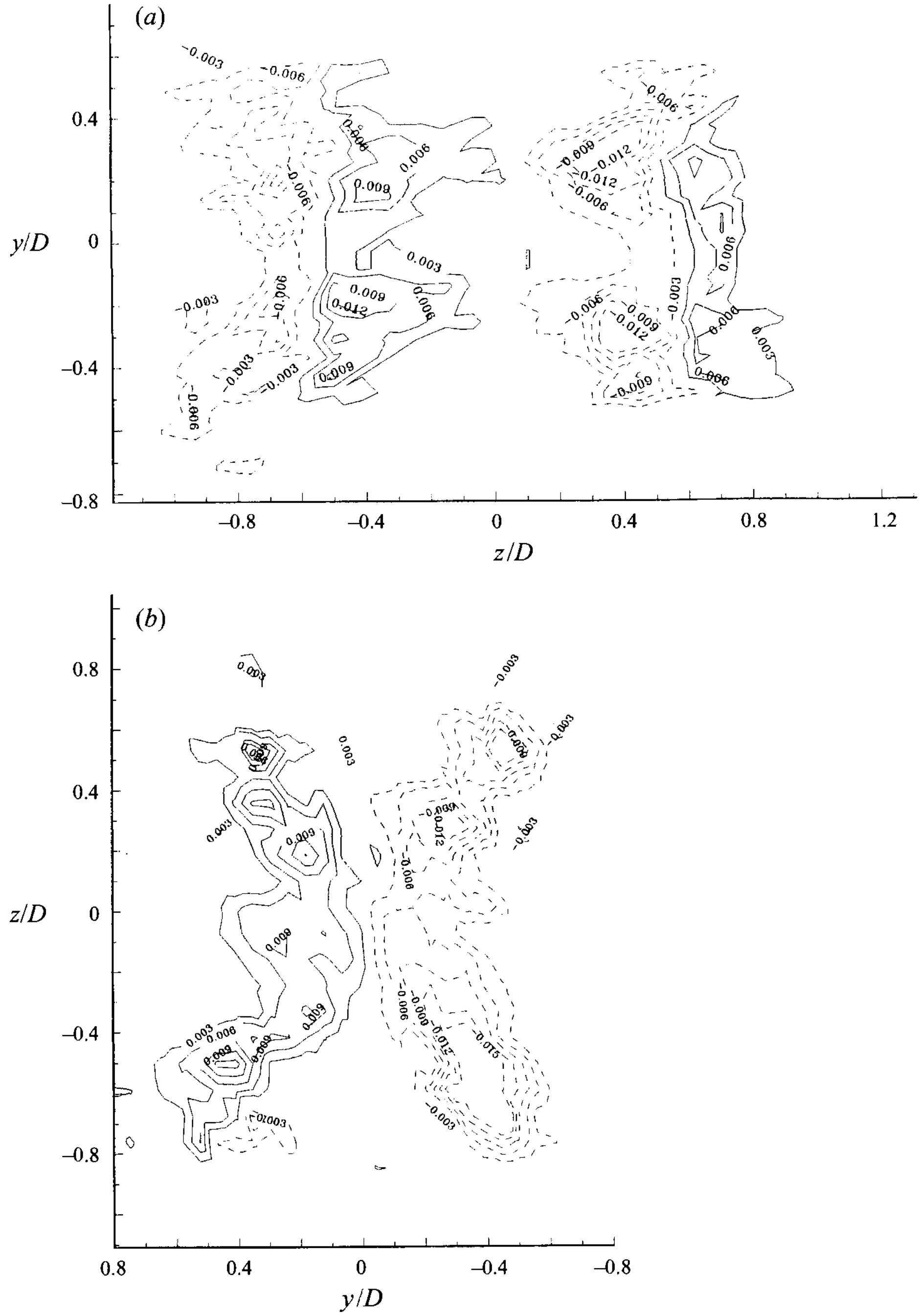

FIGURE 22. Contours of Reynolds shear stresses (a) $\overline{u'w'}$ and (b) $\overline{u'v'}$ for the two-delta-tab case (with the tabs along the y-axis) at $x/D = 2$.

from 0.06 to 0.14 between the two streamwise locations of $x/D = 1$ and $x/D = 4$. The spanwise (or for this no-tab case, radial) normal Reynolds stress, σ_v/U_{ref}, was also measured along the y-axis and is shown in figure 19(*b*). These levels rise from less than 0.02 to about 0.07–0.09 between the two streamwise stations. The Reynolds shear stress $\overline{u'v'}/U_{ref}^2$ is given in figure 19(*c*). There is a negative and a positive peak

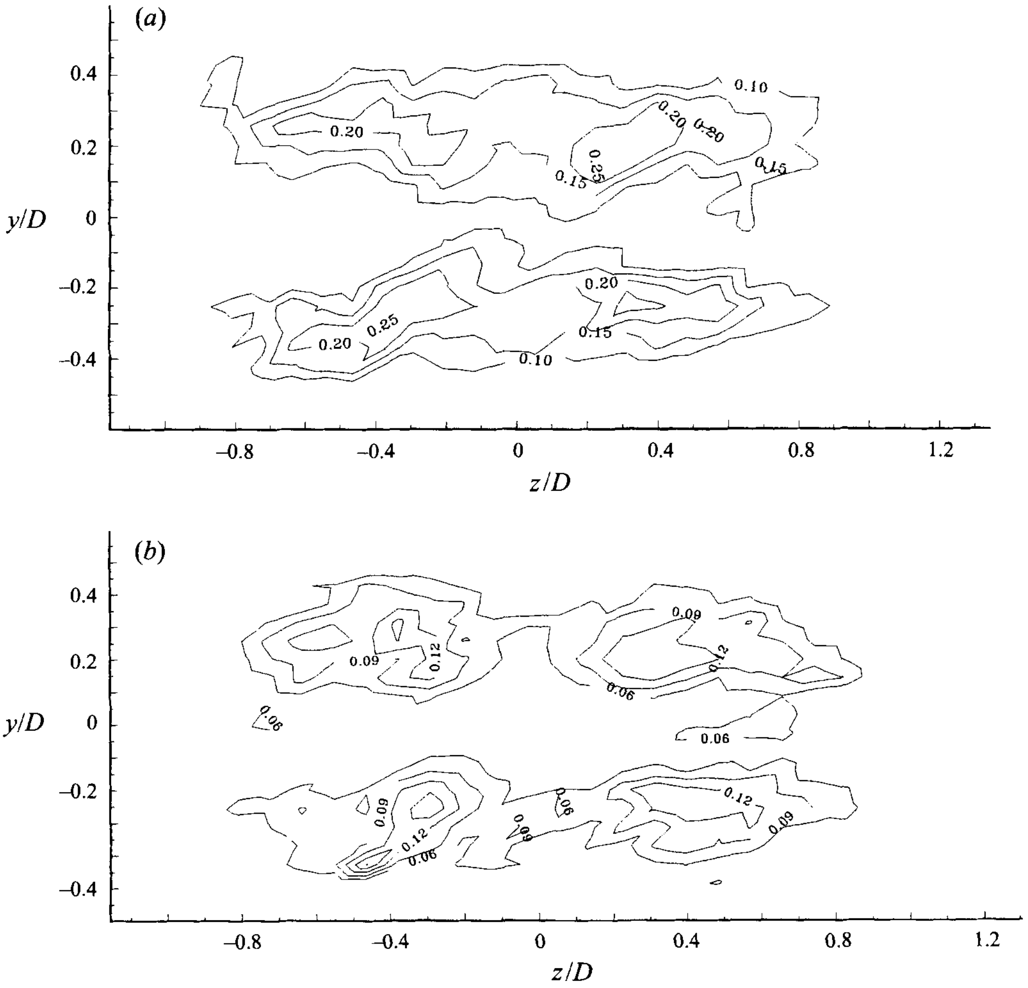

FIGURE 23(*a*, *b*). For caption see facing page.

surrounding the core of the jet, which one would expect. The levels of $\overline{u'v'}$ increase by an order of magnitude between these two stations. For these results, which are based on 2000 samples, data outside five times the standard deviation were judged to be noise and were discarded. The grid resolution was about $0.09D \times 0.06D$ for the $x/D = 2$ data and $0.11D \times 0.09D$ for the $x/D = 0.5$ data.

Streamwise normal Reynolds stresses, σ_u/U_{ref}, for the $Re = 1950$ two-delta-tab case are given in figures 20(*a*) and 20(*b*) for $x/D = 0.5$ and 2, respectively. The peak levels occur within the mixing layer, but unlike a typical round jet, the fluctuations are not uniformly dispersed about the mixing layer. The specific location of the highest magnitude fluctuations in the $x/D = 0.5$ case is near the tab tip, and the levels there are around 0.04. By $x/D = 2$ fluctuation levels have risen to just above 0.20 along the region of the mixing layer in the vicinity of the sides of the tabs. It is interesting to note that these levels substantially exceed those along the axis opposite to the tab axis. This is consistent with the mixing seen in the flow visualizations of figure 16.

In addition to streamwise Reynolds stresses, both secondary components (σ_w/U_{ref} and σ_v/U_{ref}) were measured by LDV for the $Re_D = 1950$ delta tab case. These data are given for $x/D = 2$ in figures 21(*a*) and 21(*b*), respectively. In both plots, the peak

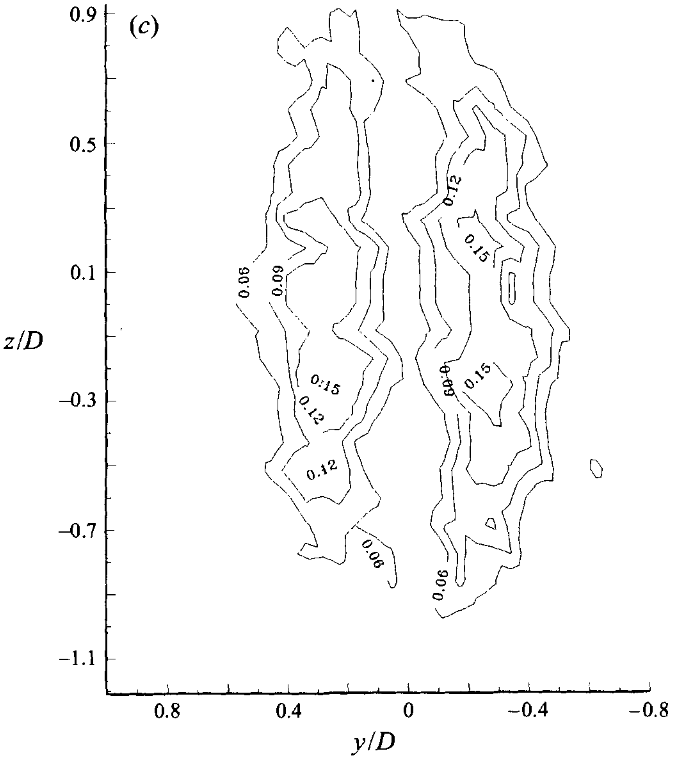

FIGURE 23. Contours of normal Reynolds stress components (*a*) σ_u, (*b*) σ_w, and (*c*) σ_v for the inverted-delta-tab case (with the tabs along the y-axis) taken at $x/D = 2$.

magnitudes have approximately the same value. It is interesting to compare the locations where the peak areas occur. As one might expect, v' fluctuations are higher along the y-axis, whereas w' values are higher along the z-axis. The peak magnitude for both σ_w/U_{ref} and σ_v/U_{ref} appears to be around 0.18 at this streamwise location ($x/D = 2$). Note that this is higher than the peaks for the no-tab case at $x/D = 4$. The importance of the spatial variations in the magnitude for σ_w/U_{ref} and σ_v/U_{ref} are further discussed in §4.

Reynolds stresses $\overline{u'w'}$ and $\overline{u'v'}$ are plotted for the $Re_D = 1950$ delta tab case in figures 22(*a*) and 22(*b*), respectively. In essence, the $\overline{u'w'}$ plots show four regions of alternating sign (two positive and two negative). These mark the direction of the shear. The strongest levels appear to be in four pockets near the sides of the two delta tabs and are twice the levels of the no-tab case taken at $x/D = 4$. Zero magnitude corresponds to the peak velocity regions in the bifurcated core. The crossover from positive to negative also occurs at the peak streamwise velocity regions for the $\overline{u'v'}/U^2_{ref}$ plots, but here there are only two regions of opposite sign. The highest magnitudes are comparable to, but slightly higher than, $\overline{u'w'}/U^2_{ref}$.

The same values (σ_u/U_{ref}, σ_w/U_{ref}, σ_v/U_{ref}, $\overline{u'w'}/U^2_{ref}$, $\overline{u'v'}/U^2_{ref}$) were obtained for the inverted delta tab case ($Re = 1950$). These are given in figures 23(*a–c*) and 24(*a*, *b*). The levels of the streamwise fluctuations are similar to that of the delta tab case at this location. Again there are four pockets of high fluctuations near the sides of the tabs. The lateral normal Reynolds stress appears considerably weaker for this case at the extreme lateral locations of the jet ($y/D > 0.4$ and $y/D < -0.4$). The spanwise normal Reynolds stress is prevalent through a longer lateral region, consistent with earlier data

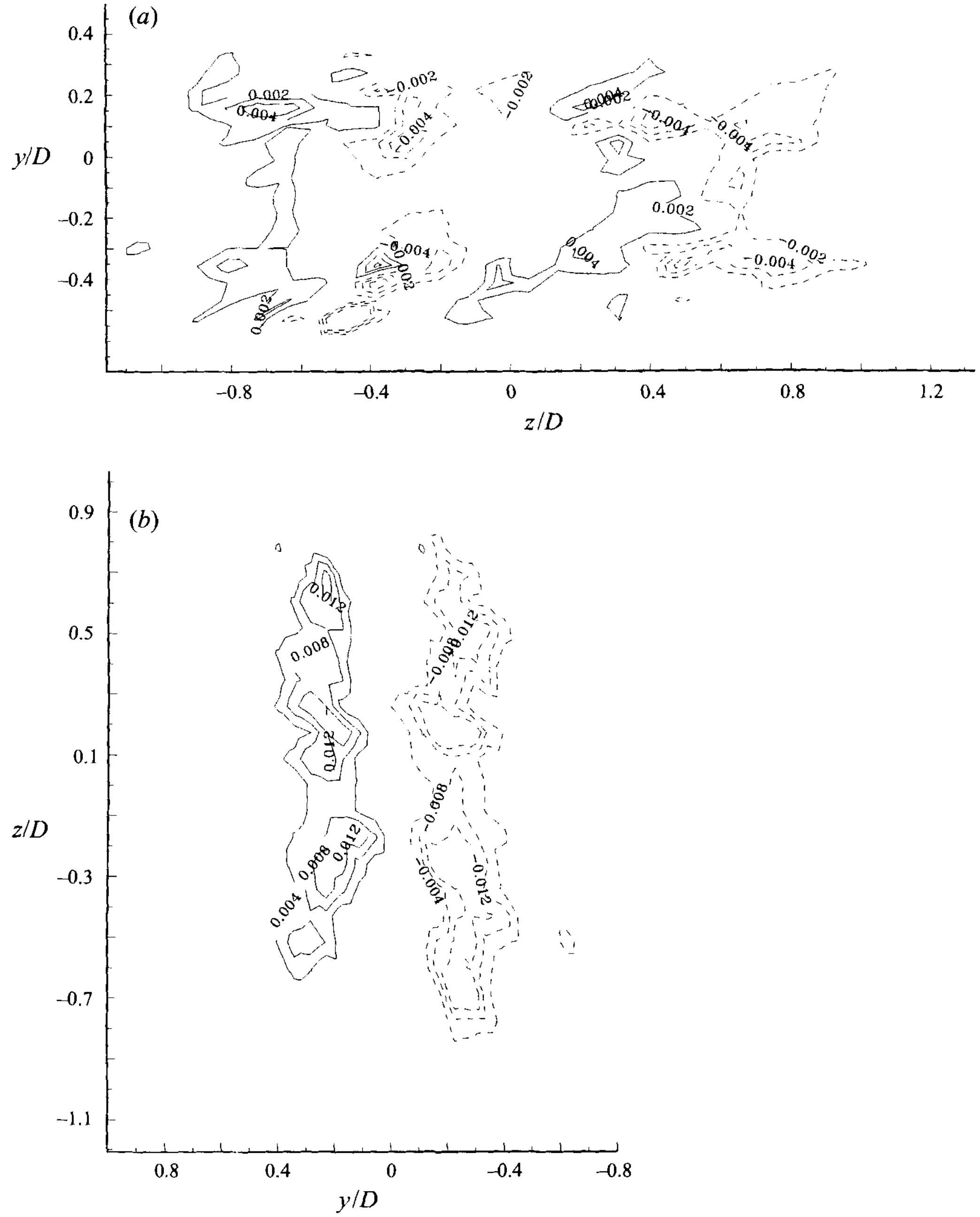

FIGURE 24. Contours of components of Reynolds shear stresses (*a*) $\overline{u'w'}$ and (*b*) $\overline{u'v'}$ for the inverted-delta-tab case (with the tabs along the y-axis) at $x/D = 2$.

showing the lengthened jet core in this direction. The Reynolds stresses once again mark the changes in the shape of the mixing layer, compared to the delta tab case. The contours in the vicinity of the tab tips are less organized and of lower value, particularly for the $\overline{u'w'}/U_{ref}^2$ data, perhaps due to the tip vortices.

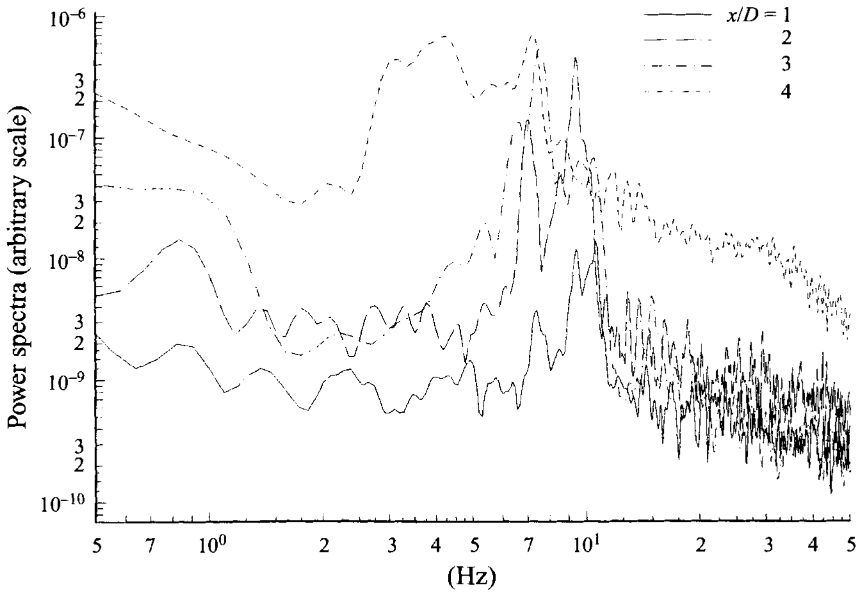

FIGURE 25. Power spectra (with arbitrary scale) derived from fluctuating lateral (and radial) velocity components within the mixing layer of an incompressible jet ($Re = 1950$) without tabs at the indicated streamwise locations.

3.5.2. *Power spectral results*

The data rate from the LDV measurements was sufficient to record spectral information. Since events generally took place on the order of 10 Hz (as seen in the flow visualizations), between roughly 10 and 100 points were recorded per full cycle. Between 6000 and 10000 data points were recorded for each measurement, so that data from several hundred cycles were averaged. While this number of points was somewhat lower than ideal, it was sufficient, and repeatability was found to be good. Typically the data rate, which was raised to at least 300 Hz for these measurements by adding more particles to both the source and ambient tanks, yielded spectral information for frequencies ranging up to from 70 to 150 Hz, based on the Nyquist criteria. The spectra were calculated using a Hanning window, and to maximize the data rate, a time-history raw data file was recorded. The spectra were calculated in this manner using the TSI (FIND™) LDV software package.

Resulting power spectra calculated from the radial velocity for the no-tab $Re_D = 1950$ case are plotted with an arbitrary scale for various streamwise locations in the mixing layer and are given in log–log form in figure 25. To minimize effects of radial location, data were recorded within the mixing layer such that the mean velocity varied only between $0.65U$ to $0.90U$. To maximize the amplitude of the disturbances in the radial velocity, these data were recorded along the y-axis.

From this figure, the trend of decreases in the frequencies of peak spectral content with increasing x/D is clearly demonstrated. The peak at 10.1 Hz for the $x/D = 1$ location yields a Strouhal number of $St_\theta = 0.016$ based on boundary layer exit momentum thickness (see table 1) and the centreline jet velocity. This corresponds well with the values found in a number of experimental and theoretical works (see Ho & Huerre 1984) to contain the most unstable and easily excitable wavelengths of the K–H instability in the initial regions of mixing layers. By $x/D = 2$, this peak has shifted to about 8 Hz, and by $x/D = 3$ the peak is at 7.2 Hz.

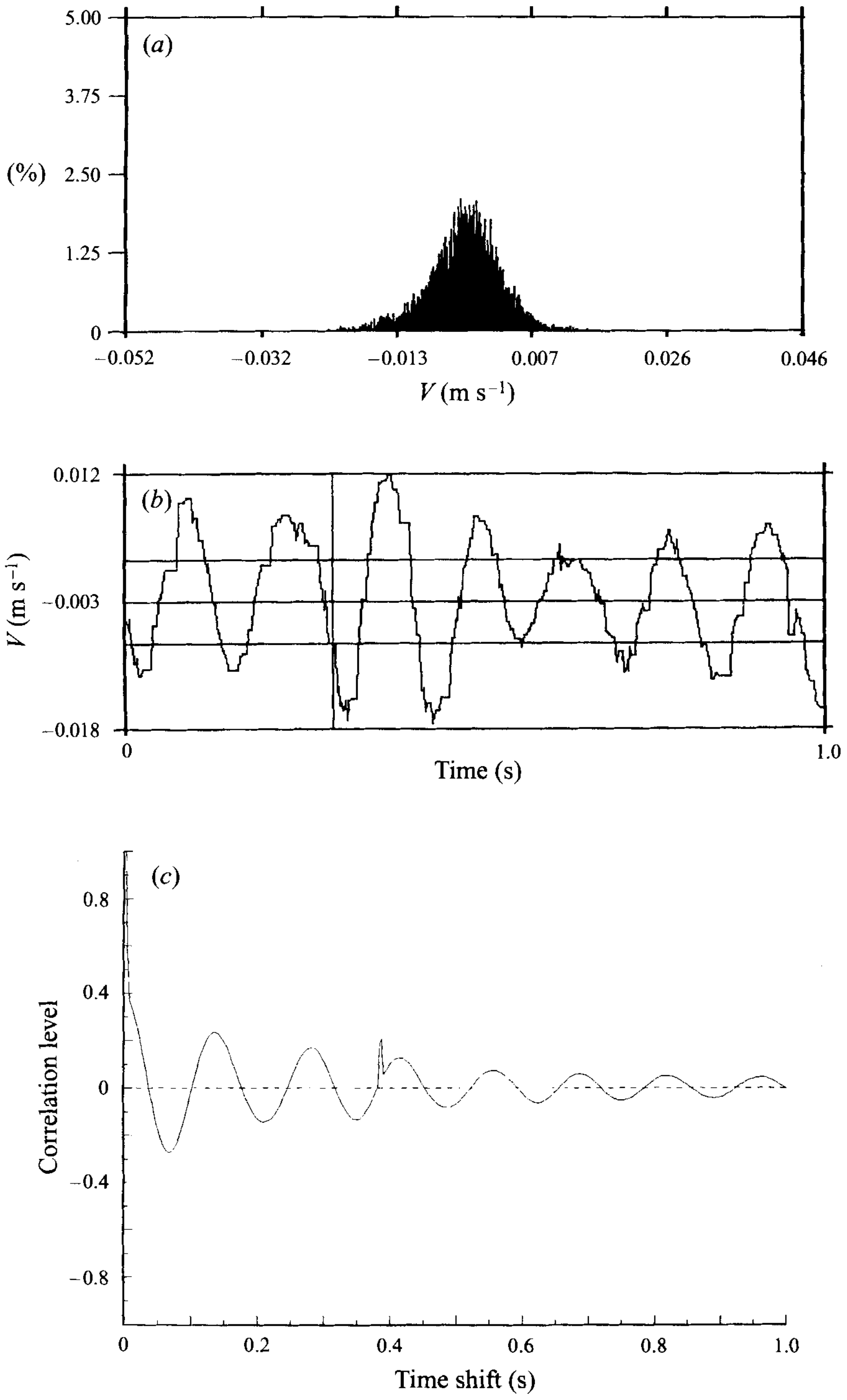

FIGURE 26. Additional details of the lateral velocity data for the $x/D = 3$ case of figure 25: (*a*) a histogram of the data, (*b*) a portion of the time signal, and (*c*) an autocorrelation of the data.

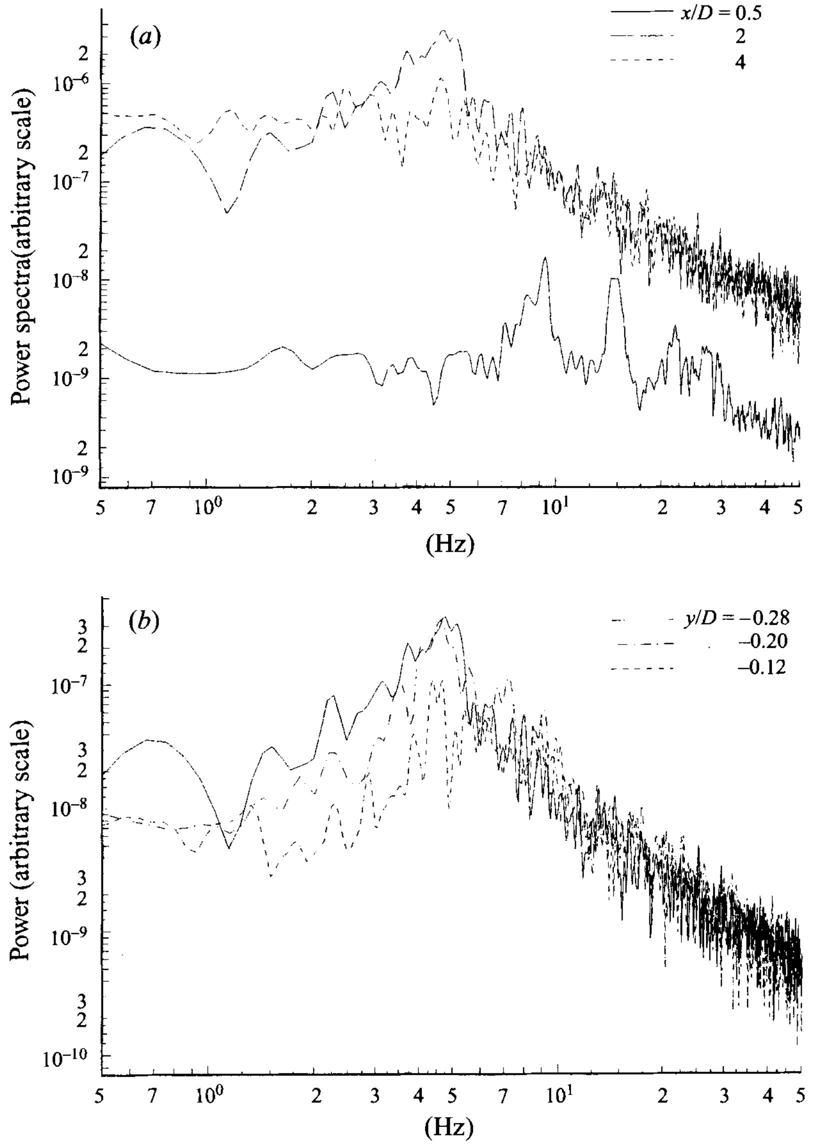

FIGURE 27. Power spectra (with arbitrary scale) derived from fluctuating spanwise velocity components within the mixing layer of an incompressible jet with two delta tabs. Data were taken on the tab axis (*a*) at the indicated streamwise locations, and (*b*) at the indicated y-locations with $x/D = 2$ and $z/D = 0$.

Additional information for the $x/D = 3$ case is given in figure 26. A histogram of the distribution of the radial velocity for this data point is given in (*a*). The relatively uniform distribution of velocities was typical for these cases. The mean secondary (i.e. radial) velocity, V, of the flow for this case was -0.003 m s^{-1} which is consistent with the location of the measurement volume within the mixing layer with $y/D < 0$. A portion of the time signal is given in (*b*) for this case. From this it is clear that the flow is quite periodic and that the time resolution is satisfactory. Within the 1 s interval, the frequency of the large-scale structures appears to be just over 7 Hz. This may be better quantified by the autocorrelation calculated using the same data, and that is given in

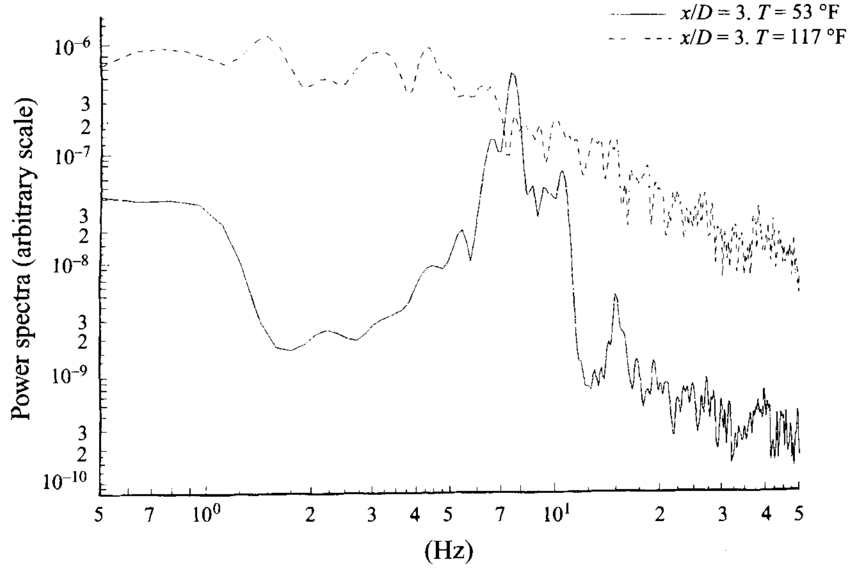

FIGURE 28. Power spectra comparison (at $x/D = 3$) of jets without tabs having different viscosities: solid line, $Re_D = 1950$; the dashed line, $Re_D = 4160$.

figure 26(*c*). The decreasing magnitude of the sinusoidal wave shows the character of the flow at this location. A very periodic flow at about 7.2 Hz with slight variations from structure to structure is indicated by this plot. Recall that the flow visualization shown in figure 14 was taken with the front sheet located at $x/D = 3$. The peak frequency at about 7.2 Hz would yield event cycling in about 8.4 frames. This is in reasonable agreement with the flow visualization which shows one cycle occurring within about 10 frames. This small discrepancy may arise because the spectral data were averaged over about 100 cycles. Thus, within reason, agreement between quantitative data and the flow visualizations is established.

Between $x/D = 3$ and 4, the peak frequency in the no-tab spectra is nearly halved from 7.2 Hz to 4.0 Hz, although a secondary peak at roughly 7 Hz remains. This may be due to coalescence of neighbouring ring vortices. At $x/D = 4$ the column mode instability of the jet becomes important (Crow & Champagne 1971). The peak at 4.0 Hz corresponds to $St_D = 0.37$ which is well within expectations from previous literature. Note that along with the decrease in frequency the peaks also broaden somewhat with increasing x/D. This is indicative of a wider distribution of mixing length scales and, in general, more disorganization in the flow.

With two delta tabs inserted along the y-axis, similarly taken spectral data were recorded for $Re = 1950$. Spectra for three streamwise locations are given in figure 27(*a*). Profound differences between this figure and the no-tab cases of figure 25 are observable. The furthest upstream point ($x/D = 0.5$) shows three regimes of peak spectral activity: one broad peak at about 20–30 Hz, one at roughly 15 Hz, and a third centred at 9.1 Hz. This indicates that there is some sort of interaction between structures, even at this early stage of the mixing layer. By $x/D = 2$ the peak spectral content is contained in a broad peak between 4 and 5.3 Hz. This corresponds to one cycle passage in about 12 frames, which is in reasonably good agreement with the dual-view flow visualizations of a single cycle in figures 15 and 16.

Comparing the $x/D = 2$ locations of figures 25 and 27(*a*), the dramatic influence of the tabs on the roll-up of K–H structures can be quantitatively assessed. The peak in

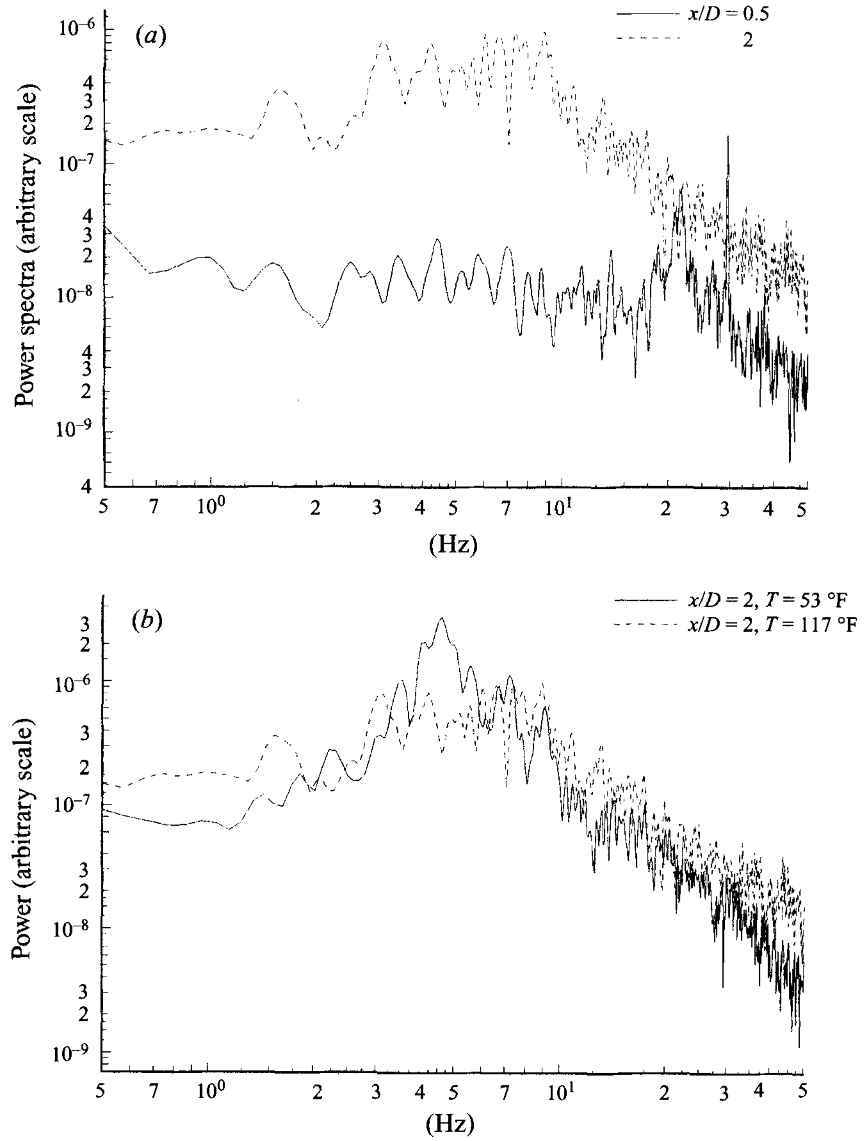

FIGURE 29. (*a*) Power spectra for the $Re_D = 4160$ jet with two delta tabs at the indicated streamwise positions and (*b*) a direct comparison of the two Reynolds number cases. Data were taken on the tab axis.

the tab case is much broader and at about half the frequency of the no-tab case. This demonstrates that the tabs cause early formation and interaction of structures within the mixing layer (at least along the tab axis), and generally cause the mixing layer to develop more rapidly. By $x/D = 4$ of the tab case, no well-defined peaks in the spectra are clearly seen.

A reasonable issue to address is whether and how the spectral content varies laterally across the mixing layer, especially in the tab cases where finer structures were apparent in flow visualizations. One might contend that the peaks in the spectra would occur at higher frequencies in the higher velocity regimes, as has been found in much higher speed mixing layers (e.g. Samimy, Reeder & Elliott 1992). However, for these low-

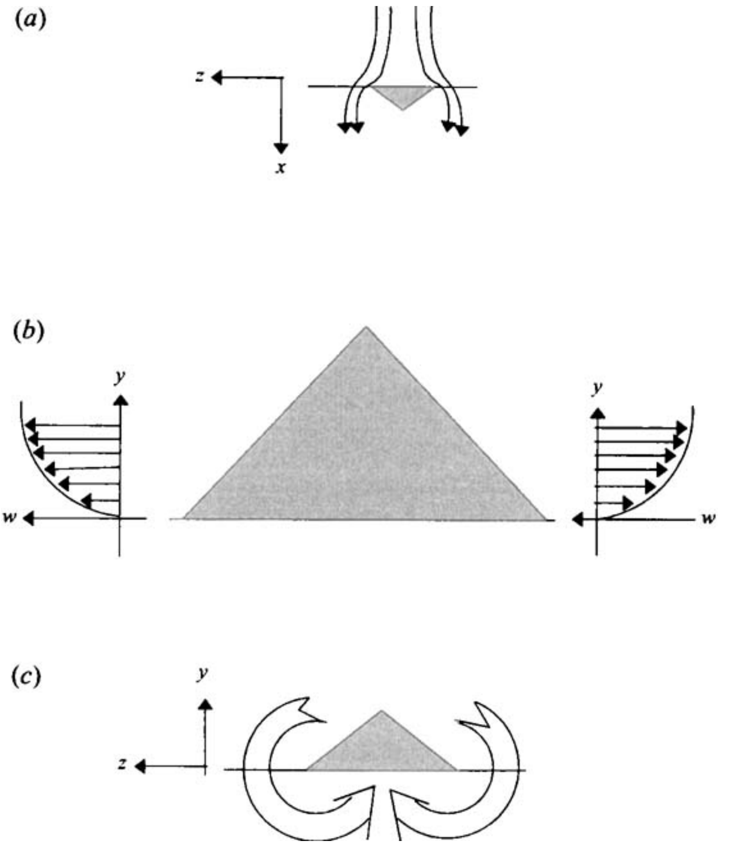

FIGURE 30. Sketch of vorticity generated by tabs along the solid surface: (*a*) a top view of a delta tab and the flow around it; (*b*) a front view of a delta tab with the generated streamwise velocity shown. The sign of the vorticity generated is given in (*c*).

speed, low-Reynolds-number jets, very little difference in the overall spectra was seen through the lateral extent of the layer, as shown in figure 27(*b*). These three locations were taken for mean velocities ranging from $0.28U_{ref}$ to $0.76U_{ref}$. While some minor differences are definitely present, the peak lies at essentially the same frequency range for each location. This is basically because large structures truly dominate this mixing layer.

Limited data were also taken for the high Reynolds number case ($T = 117$ °F, $Re_D = 4160$) for both no-tab and delta tab cases. A comparison of the two no-tab cases at $x/D = 3$ is given in figure 28. The peak seen in the lower-Re_D case is apparently much less defined for the $Re_D = 4160$ case. Considering the overall decrease in flow organization with increasing *Re*, such an effect is certainly not surprising.

For the $Re_D = 4160$ delta tab case, two streamwise locations were interrogated for spectral data and are given in figure 29(*a*). The $x/D = 0.5$ case shows two sharp peaks at roughly 20 and 28 Hz. This is in contrast to the lower Reynolds number case for this location which showed more spectral content at 10 and 15 Hz. Considering the 25% decrease in exit boundary layer momentum thickness (see table 1) for the higher Reynolds number case, an increase in the frequency of the peak content by about 25% is expected. By $x/D = 2$, the peak area has dramatically broadened. This is also seen in figure 29(*b*), which provides direct comparison of the two Re_D cases for $x/D = 2$

with delta tabs present. From here it can be seen that increasing the Reynolds number of the jet causes more disorganization in the flow, and broadens the peaks in the spectra. Notice that although the peak is broader, it occurs over roughly the same central frequency since the velocity of the jet remained constant. This disorganization, as well as the convective velocity of structures, was also demonstrated in the flow visualizations of figure 18.

4. Discussion

The source of streamwise vorticity may be described in terms of the vorticity dynamics equation for incompressible flow (see (1) below). Here, capital letters (*U*, *V*, *W*) indicate mean flow properties, fluctuating properties are primed (u', v', w'), and instantaneous values are lower case (*u*, *v*, *w*). Although the axisymmetric jet is a case where polar coordinates are intrinsic, Cartesian terminology is simpler and will be sufficient in the following analysis. This vorticity transport equation is easily derived by eliminating the pressure term between the time-averaged Reynolds equations in the *y*- and *z*-directions. As a result, streamwise vorticity production for an incompressible case may be considered without reference to pressure gradients. This is in contrast to work included in Zaman *et al.* (1994) where the streamwise vorticity distribution was described directly from pressure gradient arguments. Of course, either route is based entirely upon the basic equations of fluid motion and may be used interchangeably. The vorticity dynamics approach is used here to provide a straightforward means of understanding the formation of streamwise vortices due to tabs and to yield insight into similar flow phenomena.

The terminology of (1) follows that of Perkins (1970):

$$U\frac{\partial w_x}{\partial x}+V\frac{\partial w_x}{\partial y}+W\frac{\partial w_x}{\partial z}=\nu\nabla^2\omega_x+\underset{\mathrm{VS}}{\omega_x\frac{\partial U}{\partial x}}+\underbrace{\omega_y\frac{\partial U}{\partial y}+\omega_z\frac{\partial U}{\partial z}}_{\mathrm{P}_1}+\underset{\mathrm{P}_2}{\frac{\partial}{\partial x}\left(\frac{\overline{\partial u'v'}}{\partial z}-\frac{\overline{\partial u'w'}}{\partial y}\right)}$$

$$+\underset{\mathrm{P}_3}{\frac{\partial^2}{\partial y\,\partial z}(\overline{v'^2}-\overline{w'^2})}+\underset{\mathrm{P}_4}{\left(\frac{\partial^2}{\partial z^2}-\frac{\partial^2}{\partial y^2}\right)\overline{v'w'}}, \quad (1)$$

where $$\omega_x=\frac{\partial W}{\partial y}-\frac{\partial V}{\partial z},\quad \omega_y=\frac{\partial U}{\partial z}-\frac{\partial W}{\partial x},\quad \omega_z=\frac{\partial V}{\partial x}-\frac{\partial U}{\partial y}.$$

The first term on the right-hand side of (1) is the viscous diffusion term and the second term represents streamwise vortex stretching (VS). The subsequent two terms, referred to as P_1, describe secondary flow production of the first kind. The remaining three terms (P_2, P_3, and P_4) comprise secondary flow production of the second kind. Bradshaw (1987) briefly comments on the equivalent aspects of the 'secondary flow' and 'streamwise vorticity', and either may be referred to in this discussion.

Consider the flow around a tab. Figure 30 shows a simple sketch of what occurs, neglecting wall curvature. In order to get past the tab, the flow must acquire a velocity (*W*) in the *z*-direction. Moreover, consider what form the velocity *W* would take along the *y*-direction locations adjacent to the tab. This is sketched in figure 30(*b*) where it is noted that $W=0$ at the wall due to the no-slip condition and increases with distance from the wall. Very close to the solid nozzle wall the velocity (*V*) in the *y*-direction

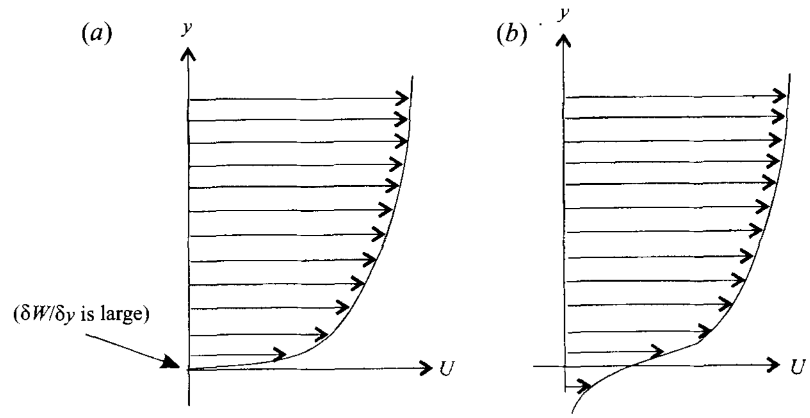

FIGURE 31. Increased streamwise velocity intensifies the streamwise vorticity shown in figure 30 via vortex stretching: (a) a typical bounded flow, (b) the early mixing layer.

(normal to the wall) is much less than W. Thus, it is reasonable to assume that the streamwise vorticity ω_x is simply $\partial W/\partial y$ and is a significant quantity at the wall. In Prandtl's (1952) terminology, this may be considered streamwise vorticity production of the first kind since the spanwise vorticity is skewed by $\partial U/\partial z$ (Bradshaw 1987). Notice that the sense of rotation of the vorticity is the same as that measured using LDV and which would cause the jet deformation shown.

The degree of deformation of the jet observed in these figures is consistent with intense streamwise vorticity. This is thought to be brought about by the vortex stretching term in (1). Consider the streamwise velocity in the boundary layer adjacent to the tab just before the jet exit as shown in figure 31(*a*). In comparing figures 30(*b*) and 31(*a*), one observes that at the spatial locations where $\partial W/\partial y$ is near a maximum, U is near its minimum. This occurs at the wall. Where the solid wall ends and the free shear layer begins, U near the wall is no longer restricted by the no-slip condition and grows from virtually zero to a significant fraction of the centreline velocity as sketched in figure 31(*b*) (and verified earlier in figure 4). This acceleration of the mean flow in the region nearest the wall is due not only to viscous diffusion, but also to the fluctuations induced by the Kelvin–Helmholtz instability. While this increase may not seem dramatic, it represents an order of magnitude if regions very close to the nozzle exit wall are considered. Since both ω_x and $\partial U/\partial x$ are prominent at the same locations (i.e. near the wall at the nozzle exit), the vortex stretching term $\omega_x \partial U/\partial x$ is large. Thus, the streamwise vortices intensify with streamwise distance in the early part of the jet mixing layer development region. This description of the importance of stretching is consistent with earlier work (e.g. Jimenez 1983; Bell & Mehta 1993) which demonstrated that minuscule irregularities on the trailing edge of a splitter plate provide sites for streamwise vortices far downstream.

These principles may be applied to unravel the underlying reasons for many of the properties exhibited by tabs observed both in earlier and in the present experiments. Delta tabs deform the jet more than simple rectangular tabs partly because of their broader base. This would cause additional boundary layer skewing leading to stronger vortices. The second reason may be understood by considering the term $\partial V/\partial z$. By sweeping the tab tip downstream, this term contributes to the streamwise vorticity generated by the $\partial W/\partial y$ term (on the same side of the tab). By contrast, the inverted delta tabs generate a second set of vortices near the tab tip since the $\partial V/\partial z$ term is

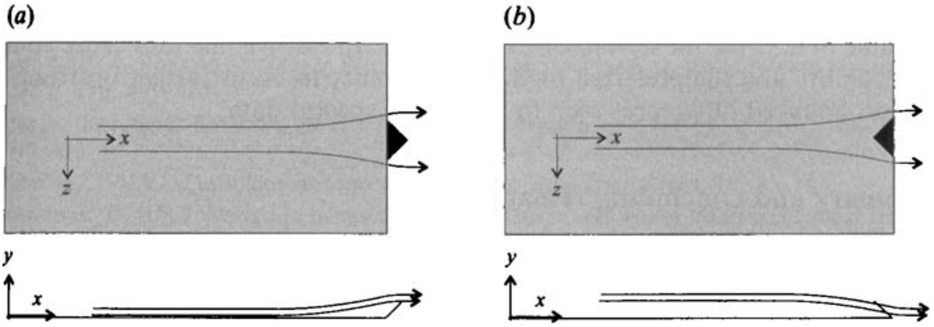

FIGURE 32. Vorticity dynamics may be used to explain the effect of (*a*) delta tabs and (*b*) inverted delta tabs.

opposite to the $\partial W/\partial y$ term in this instance. The concept is sketched in figure 32. It is apparent that the effect of the $\partial V/\partial z$ term is weaker than the turning of the boundary layer and is localized near the tip of each inverted delta tab.

Another source of streamwise vorticity is the horseshoe vortex pair generated by each tab. This vortex pair is generated as the spanwise vortex lines are wrapped around the tab. From a downstream vantage point, this results in the appearance of rolled-up streamwise vortices. Their presence outside the trailing vortices which substantially deform the flow are consistent with observations in three-dimensional boundary layer flows with obstables extending from the boundary (e.g. Acarlar & Smith 1987; Andreopoulous & Rodi 1984). These references pertain to vastly different flow fields from the one studied here, but in each the horseshoe (a.k.a. 'bound' or 'standing') vortices appear outside (i.e. further away from the obstable along the z-axis) the 'trailing' type vortices in the flow. The likely reason why these horseshoe vortices were not seen in earlier work with tabs in high-speed flow is that in the present experiments the boundary layer thickness is an order of magnitude larger.

Along with generating streamwise vortices, the tabs also influence the development of the K–H roll-up. A tab projecting into the free stream causes both a variation in effective jet curvature and also a disruption in the boundary layer along its surface. Since the frequency (or length scale) of the initial K–H roll-up varies linearly with the nozzle exit boundary layer momentum thickness, a thinning of the boundary layer on the tab surface would tend to generate higher frequencies. Another contributing factor in a tab's effect on coherent structure formation is the variation in the local radius of curvature at the nozzle exit. At locations near a tab, this radius would become smaller. This would also cause fluctuations in the mixing layer at higher frequencies, and they would begin farther upstream than for a no-tab case.

Recall that in the side views of the incompressible jet, a swept back structure can be identified as it convects downstream. The highly mixed areas toward the central axis of the images are due to the earlier development of structures in the vicinity of a tab. The fact that individual structures appear curved, with the region near the tab tip advanced slightly farther downstream, may also be attributed to the response of individual structures to these local curvature variations. A smaller radius, such as that in the vicinity of a tab, has been shown, e.g. by Hussain & Husain (1989), to increase the local convection speed of a structure. This would explain the advancement of individual structures near a tab tip.

The changes in structure evolution due to tabs also seem to affect the preferred mode jet instability. This is evident by the lower frequency of naturally occurring structures (at a given streamwise location) for tab cases. By $x/D = 2$, $St_D = 0.38$, which compares to the value of 0.37 for the no-tab case at $x/D = 4$. In essence, the tabs cause both the K–H instability and the preferred mode jet instability to occur farther upstream and lead to pronounced differences seen in the power spectra data.

5. Summary and concluding remarks

The effect of vortex-generating tabs on an axisymmetric jet has been illustrated in flow visualizations and has been extensively probed using two-component velocity measurements. The overall pattern of distortion detected in the low-speed water jet, detected through visualizations and detailed velocity data, was consistent with earlier observations in high-speed jets. Secondary velocity measurements demonstrated that a pair of strong counter-rotating streamwise vortices were generated by each tab. In addition, a second set of streamwise vortices, which correspond to a horseshoe vortex system, were generated by each delta tab. This second set of vortices was not seen in previous work, probably due to the thinner nozzle exit boundary layers for high-speed jets. For the case of inverted delta tabs, yet a third set of streamwise vortices were generated near the tip of each tab.

Dual-view real-time flow visualizations illustrated the periodic vortex ring roll-up in an axisymmetric jet with $Re_D = 1950$. By simultaneously viewing the evolution of jets from two orthogonal perspectives, much insight into the mixing was gained. When tabs were inserted, the evolution of periodic flow structures was drastically altered. The action of the streamwise vortices generated by each tab caused a marked increase in the ambient fluid entrained into the jet. This enhancement of mixing was indicated by both the flow visualizations and by the higher Reynolds stress levels for the tab cases. The changes in the periodic structure seen in the visualizations were also witnessed in real-time velocity data which yielded spectral information about the flow.

The means by which streamwise vorticity is generated by tabs was described using vortex dynamics. By considering how the tabs turn the flow near the boundary (streamwise vorticity production of the first kind), the primary effect of tabs may be understood. The presence of streamwise vorticity very near the wall at the nozzle exit is especially significant when the effect of the vortex stretching term is considered. This approach was also used to demonstrate why the inverted delta tabs generate tip vortices.

The authors would like to acknowledge the support of NASA grant NAG3-764 and contract monitor Dr Khairul Zaman for many helpful discussions. In addition we would also like to thank the reviewers for their helpful suggestions which substantially enhanced the quality of the paper.

REFERENCES

Acarlar, M. S. & Smith, C. R. 1987 A study of hairpin vortices in a laminar boundary layer. Part 1. Hairpin vortices generated by a hemisphere protuberance. *J. Fluid Mech.* **175**, 1–41.

Ahuja, K. K. & Brown, W. H. 1989 Shear flow control by mechanical tabs. *AIAA Paper* 89-0994.

Andreopouolos, J. & Rodi, W. 1984 Experimental investigation of jets in crossflow. *J. Fluid Mech.* **138**, 93–127.

Ashurst, W. T. & Meiburg, E. 1988 Three-dimensional shear layers via vortex dynamics. *J. Fluid Mech.* **189**, 87–116.

Bell, J. H. & Mehta, R. D. 1992 Measurements of the streamwise vortical structures in a plane mixing layer. *J. Fluid Mech.* **239**, 213–248.

Bell, J. H. & Mehta, R. D. 1993 Effects of spanwise perturbations on plane mixing-layer structure. *J. Fluid Mech.* **257**, 33–63.

Bernal, L. P. & Roshko, A. 1986 Streamwise vortex structures in plane mixing layers. *J. Fluid Mech.* **170**, 499–525.

Bradbury, L. J. S. & Khadem, A. H. 1975 The distortion of a jet by tabs. *J. Fluid Mech.* **70**, 801–813.

Bradshaw, P. 1987 Turbulent secondary flows. *Ann. Rev. Fluid Mech.* **19**, 53–74.

Breidenthal, R. 1981 Structure in turbulent shear layers and wakes using a chemical reaction. *J. Fluid Mech.* **109**, 1–24.

Browand, F. K. & Troutt, T. R. 1980 A note on spanwise structure in the two-dimensional mixing layer. *J. Fluid Mech.* **97**, 771–781.

Brown, G. L. & Roshko, A. 1974 On density effects and large structure in turbulent mixing layers. *J. Fluid Mech.* **64**, 775–816.

Cantwell, B. J. 1981 Organized motions in turbulent flow. *Ann. Rev. Fluid Mech.* **13**, 457–515.

Corcos, G. M. & Lin, S. J. 1984 The mixing layer: deterministic models of turbulent flow. Part 2: the origin of three-dimensional motion. *J. Fluid Mech.* **139**, 67–95.

Crow, S. C. & Champagne, F. H. 1971 Orderly structure in jet turbulence. *J. Fluid Mech.* **48**, 547–591.

Dimotakis, P. E., Miake-Lye, R. C. & Papantoniou, D. A. 1983 Structure and dynamics of round turbulent jets. *Phys. Fluids* **26**, 3185–3192.

Ho, C. M. & Huerre, P. 1984 Perturbed free shear layers. *Ann. Rev. Fluid Mech.* **16**, 365–424.

Hussain, F. & Husain, H. S. 1989 Elliptic jets. Part 1. Characteristics of unexcited and excited jets. *J. Fluid Mech.* **206**, 257–320.

Jimenez, J. 1983 A spanwise structure in the plane shear layer. *J. Fluid Mech.* **132**, 319–336.

Konrad, J. H. 1976 An experimental study of mixing in two-dimensional turbulent shear flows with applications to diffusion limited chemical reactions. *Project SQUID Tech. Rep.* CIT-8-PU.

Lasheras, J. C., Cho, J. S. & Maxworthy, T. 1986 On the origin and evolution of streamwise vortical structure in a plane, free shear layer. *J. Fluid Mech.* **172**, 231–258.

Lasheras, J. C. & Choi, H. 1988 Three-dimensional instability of a plane free shear layer: an experimental study of the formation and evolution of streamwise vortices. *J. Fluid Mech.* **189**, 53–86.

Liepmann, D. & Gharib, M. 1992 The role of streamwise vorticity in near-field entrainment of round jets. *J. Fluid Mech.* **245**, 643–668.

Longmire, E. K., Eaton, J. K. & Elkins, C. J. 1992 Control of jet structure by crown-shaped nozzles. *AIAA J.* **30**, 505–512.

Martin, J. E. & Meiburg, E. 1991 Numerical investigation of three-dimensionally evolving jets subject to axisymmetric and azimuthal perturbations. *J. Fluid Mech.* **230**, 271–318.

Perkins, H. J. 1970 The formation of streamwise vorticity in turbulent flow. *J. Fluid Mech.* **44**, 721–740.

Pierrehumbert, R. T. & Widnall, S. E. 1982 The two- and three-dimensional instabilities of a spatially periodic shear layer. *J. Fluid Mech.* **114**, 59–82.

Prandtl, L. 1952 *Essentials of Fluid Dynamics*, pp. 145–149. Hafner Publishing Co.

Reeder, M. F. & Zaman, K. B. M. Q. 1994 The impact of 'tab' location relative to the nozzle exit on jet distortion. *AIAA Paper* 94-3385.

Reynolds, W. C. & Carr, L. W. 1985 Review of unsteady, driven separated flows. *AIAA Paper* 85-0527.

Samimy, M., Reeder, M. F. & Elliott, G. S. 1992 Compressibility effects on large structures in free shear flows. *AIAA J.* **4**, 1251–1258.

Samimy, M., Zaman, K. B. M. Q. & Reeder, M. F. 1993 Effect of tabs on the flow and noise field of an axisymmetric jet. *AIAA J.* **31**, 609–619.

Tanna, H. K. 1977 An experimental study of jet noise. Part 2: shock associated noise. *J. Sound Vib.* **50**, 429–444.

Tillman, T. G., Paterson, R. W. & Presz, W. M. 1992 Supersonic mixer ejector. *J Propulsion and Power* **8**, 513–519.

WINANT, C. D. & BROWAND, F. K. 1974 Vortex pairing: the mechanism of structure growth at moderate Reynolds number. *J. Fluid Mech.* **63**, 237–255.

WISHART, D. P., KROTHAPALLI, A. & MUNGAL, M. G. 1993 Supersonic jet control via point disturbances inside the nozzle. *AIAA J.* **31**, 1340–1341.

YODA, M., HESSELINK, L. & MUNGAL, M. G. 1992 The evolution and nature of large-scale structures in the turbulent jet. *Phys. Fluids* A **4**, 803–811.

YULE, A. J. 1978 Large scale structure in the mixing layer of a round jet. *J. Fluid Mech.* **89**, 413–432.

ZAMAN, K. B. M. Q. 1993 Streamwise vorticity generation and mixing enhancement in free jets by 'delta tabs'. *AIAA Paper* 93-3253.

ZAMAN, K. B. M. Q., REEDER, M. F. & SAMIMY, M. 1994 Control of an axisymmetric jet using vortex generators. *Phys. Fluids* **6**, 778-793.